CHALMERS
UNIVERSITY OF TECHNOLOGY

Operando Investigations of Deposition Mechanisms in Li-metal batteries

Master's thesis in Physics

ARNITA SPULE

DEPARTMENT OF PHYSICS

CHALMERS UNIVERSITY OF TECHNOLOGY
Gothenburg, Sweden 2021
www.chalmers.se

Operando Investigations of Deposition Mechanisms in Li-metal Batteries

ARNITA SPULE

Supervisors: Aleksandar Matic, Division of Materials Physics
Matthew Sadd, Division of Materials Physics

Examiner: Aleksandar Matic, Division of Materials Physics

Master's Thesis 2021

Department of Physics
Division of Materials Physics
Chalmers University of Technology
SE-412 96 Gothenburg

ABSTRACT

Lithium-ion batteries today are widely used in laptops, smartphones, electric vehicles, and other devices. However, due to the increasing demand for high energy density storage systems, one should look beyond this current state-of-the-art technology. One concept is to use Li-metal as anode material instead of graphite. Its use is promising because of its ultra-high theoretical specific capacity, 3860 mAh/g vs 372 mAh/g for graphite, and low potential of -3.04 V vs Standard Hydrogen Electrode (SHE). However, several drawbacks limit the commercialization of Li-metal batteries, such as a low coulombic efficiency (CE) and dendrite growth, which causes safety issues. To suppress dendrite growth and have high CE, uniform Li-metal deposition at charging is crucial. One of the approaches to obtain high CE is by optimizing the electrolyte composition. In literature, it has been shown that the use of $LiNO_3$ as an additive within the electrolyte improves the CE and leads to stable cycling; however, the detailed mechanism and link to the deposition process is still unclear.

To investigate the impact of the $LiNO_3$ additive within the electrolyte in Li-metal batteries, Li-Cu cells were assembled and galvanostatically cycled. It was observed that with an increase of $LiNO_3$ concentration, coulombic efficiency and cycling stability were increased. *Operando* X-ray Tomographic Microscopy was performed to link the electrochemical results to the morphology of deposited Li-metal. The results show a clear difference in the morphology of deposited Li between the systems with and without $LiNO_3$ added to the electrolyte. The Li-deposition morphology with added $LiNO_3$ is uniform and dense whereas without $LiNO_3$ it is sparse and clearly dendritic.

ACKNOWLEDGEMENTS

First, I would like to express my highest gratitude to Professor Aleksandar Matic, who first inspired me in the study course, “Functional Energy Materials,” with exciting insights into the fundamentals of batteries. I thank him also for so enthusiastically and supportively agreeing to host me as a member of his group for thesis work when I wanted to explore the field of batteries more!

I am also beyond thankful for my supervisor Matthew Sadd, who provided me tremendous support and led me through all struggles, both theoretical and practical, with wise advice always.

I am countlessly thanking all the members of Chalmers (K)MF research group, especially for being so warm-welcoming and giving me endless inspiration during our many discussions, meetings, and Fikas.

I am very grateful to be involved in the Erasmus+ mobility program, without which this journey would not be possible. Despite the crazy times we live in right now, I have still had a unique and fascinating experience.

Finally, I could not make it without the support of my family and friends, who supported me endlessly being 700+ km’s away and believed in me even when I did not believe in myself.

TABLE OF CONTENTS

1. INTRODUCTION

Nowadays, our life would be incomprehensible without smartphones, cameras, laptops, cars, and many other personal devices powered by batteries. Batteries are also central as energy storage comes in the challenge to develop more sustainable energy systems to decrease CO_2 emissions to prevent global warming and avoid depleting fossil resource usage [1]. Since the 1990s, the state-of-the-art solution for efficient energy storage is the lithium-ion battery (LIBs) that utilizes a graphite anode. They are used in electric vehicles, laptops, smartphones, and other devices due to their considerable variation in design and shape [2,3], their high reversibility and long cycle life [4]. However, LIB technology is reaching its limits in energy density, therefore to meet the demands of new applications, it is crucial to think beyond current technologies [1,3]. Other concerns are sustainability and costs of the materials utilized in battery systems [3].

For the Next Generation Batteries (NGBs) such as lithium-air (Li-O_2), lithium-sulfur (Li-S), and solid-state batteries, the use of Li-metal as an anode is considered. It has a theoretical specific capacity reaching 3860 mAh/g, is 10 times higher than graphite (372 mAh/g) [1,5] and could boost the energy density of Li-batteries. However, it has drawbacks that hinder commercialization, such as low reversibility and safety hazards (short-circuits, thermal runaways, etc.) [5]. To overcome those challenges, it is crucial to find strategies to increase reversibility and reduce safety hazards, and the foundation for this is to understand the mechanisms that trigger and cause these problems to move forward to develop novel solutions [6,7].

There are several methods found in the literature that claim to improve the performance of Li-metal anodes in terms of reversibility by, for example, adjusting the formulation of the electrolyte, modification of the separator or the electrodes and, engineering the solid electrolyte interphase (SEI) [5]. A strategy that is considered and studied particularly within this thesis is the addition of $LiNO_3$ as additive to the electrolyte. The results reported in literature seem promising [8]; nevertheless, the performance is still not sufficient to meet requirements for commercialization, for example, for automotive applications [9]. The precise mechanism of why and how $LiNO_3$ improves the Li-metal battery's performance is not yet understood.

To unveil the mechanism of stabilization by $LiNO_3$, in this work, Li-Cu cells were assembled with various $LiNO_3$ concentration and galvanostatically cycled. Complementing these experiments, *operando* Tomographic Microscopy imaging was performed to investigate the morphology of deposited Li-metal. It is a very convenient method providing in-depth information at the same time as being non-destructive [10,11]. The aim of this work, is to correlate

the electrochemical and tomography data to add understanding of the role of $LiNO_3$ for Li-metal anodes.

1.1. Background

Even though the world is facing global warming and the gradual depletion of fossil-fuel resources, society is not ready to refuse the comfort that modern technologies provide. Based on statistics as shown in Fig. 1.1. the population is growing, and so is the energy consumption [1,2]. It is predicted that by the year 2050, demand will be increased to 28 TW, and that must be met without increasing carbon dioxide emissions [1].

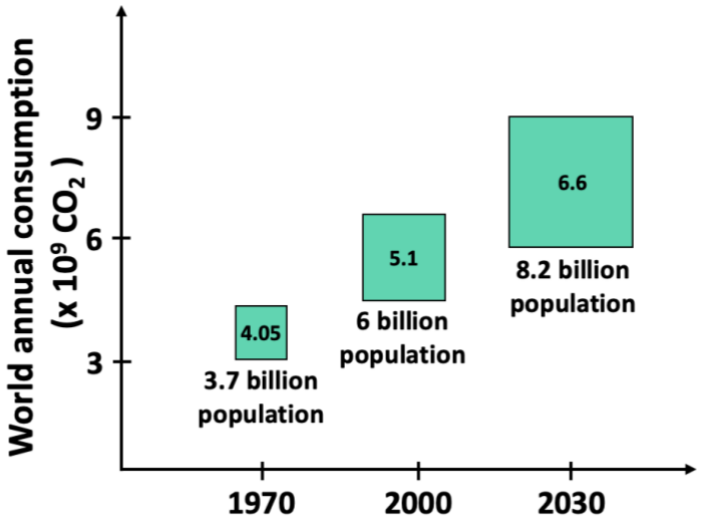

Fig. 1.1. Forecast of the World Demand for energy up to the year 2050 [1]

There are various power sources apart fossile – waste combustion, nuclear energy, and renewable sources such as hydro and wind [1]. Fig. 1.2. shows how heavily the amount of CO_2 emissions from electric vehicles relies on the way the electricity is produced. Apart from when it is 100 % produced of coal, it is more environmentally friendly in terms of CO_2 emissions compared to diesel and gasoline [1].

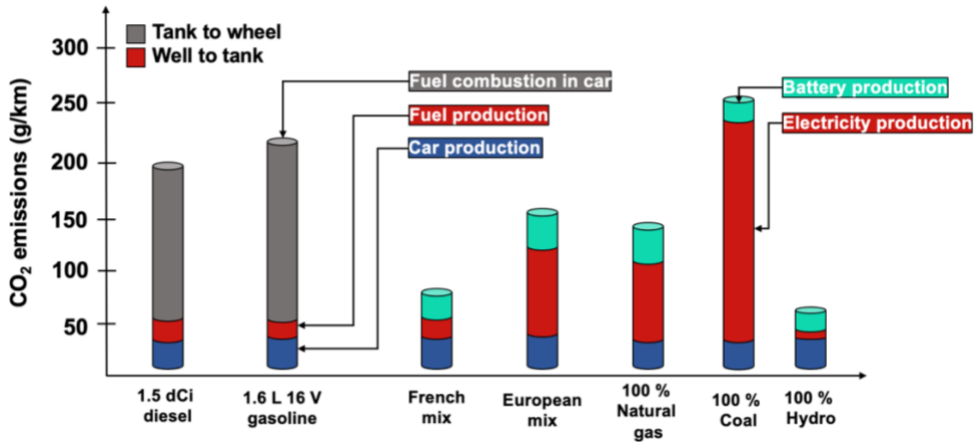

Fig. 1.2. Amount of CO_2 emissions produced depending on the sources used as a fuel [1]

1.2. Fundamentals of a battery and electrochemical metrics

To understand the electrochemical processes in a battery, thermodynamics must be introduced as well as the most commonly used metrics that characterize the overall performance of the battery system. The term cell will be used here instead of a battery, as the battery in practice consists of cells stacked together [12].

The main prerequisite for any system to do any kind of work is that a driving force must be present – either spontaneous or applied. The driving force required for the cell to work is that there must be a potential difference between electrodes [12]. The total energy of the cell is given by the Gibbs free energy:

$$\Delta G = -nFE_{cell} \tag{1.1.}$$

where n is the number of electrons transferred (per mole reactant), F is Faraday's constant and E^0_{cell} is equilibrium cell voltage. Assuming that reversible reactions occur within the cell:

$$O + ne^- \rightleftarrows R \tag{1.2.}$$

the Nernst-equation

$$E_e = E_e^0 + \frac{2.3\,RT}{nF} log \frac{c_O}{c_R} \tag{1.3.}$$

takes into account the concentrations of components O (oxidised species) and R (reduced species) and thereby determines the potential of an electrode [12]. At equilibrium – both reduction from O to R and oxidation from R to O occur at the same rate. As soon as current is applied, the concentration of O and R species changes; thus, there will be a change in the observed potential. Consequently total voltage of the cell can be determined by knowing E_e for each electrode – cathode and anode [12]:

$$E_{cell} = E_c - E_a \tag{1.4.}$$

Practically cell consists of two electrodes – cathode and anode and a separator soaked with an electrolyte. The separator acts as a physical barrier between the electrodes to prevent short-circuiting and the electrolyte ensures that ions can move between electrodes during

charge and discharge. Both the electrolyte and the separator have to be electrically insulating to prevent electrons from passing through, so they are pushed through an external circuit [3,4,12].

Fig. 1.3. shows the working principle of a cell. At discharge, spontaneous oxidation (loss of electron) on anode occurs and ions travel to cathode, releasing the electron in an external circuit where reduction (gain of electron) on cathode then happens. To charge the cell, current is applied and ions are then pushed from cathode to anode, initiating a reduction at the anode and oxidation on the cathode [3].

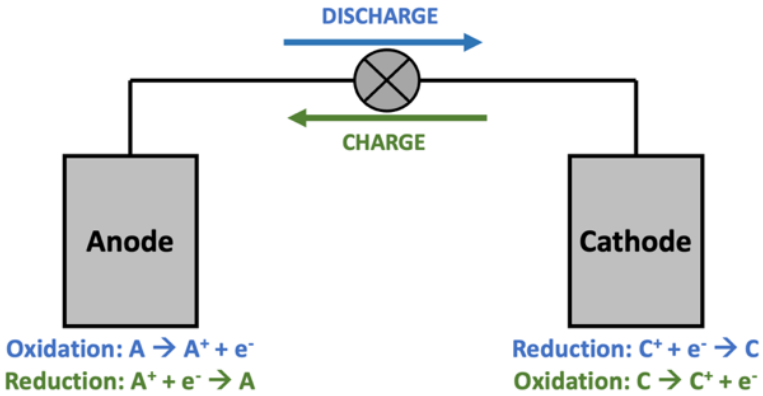

Fig. 1.3. Basic working principle of the cell

Regarding electrochemical metrics that characterize cell performance, one of the most important is the cell voltage (V). Through the experiments within this thesis, voltage profiles were obtained by galvanostatic cycling, which means that the applied current was controlled while the cell voltage was measured [3]. To determine the current that should be applied, the parameter current density is used, which is applied current per area (mA/cm^2). Taking into account both applied current density and time, the areal capacity (mAh/cm^2) can be determined [13]. In literature, the specific capacity (mAh/g) is often as a measure of the capacity of a material [14]. An essential term is also the gravimetric energy density (Wh/kg) [15]. All the metrics and units are summarised in Table 1.1. Another crucial parameter to determine cell performance is the coulombic efficiency (CE), defined as the ratio of discharge capacity to the charge capacity [16,17].

The nucleation potential is a parameter that provides information about how much excess energy (overpotential) is required to initiate electrodeposition of one material on a substrate [13]. Within this thesis, lithium is plated on copper during discharge. The determination of $V_{nuc.\ pot.}$ is challenging due to various processes that contribute to the overpotential and cannot easily be distinguished. Such processes are – mass transport (where ions travel through the electrolyte and through the SEI layer), charge transfer (where Li-ions gets reduced, forming

metallic Li on the Cu surface), and Li-ion adsorption on the surface as well as crystallization (as soon as the critical size of a nucleus is reached). The main contributing processes to the nucleation potential are Li-ion adsorption and crystallization; however, there is still a lack of methods to distinguish these processes; that is why the overpotential minimum during nucleation will be assumed as the nucleation potential within this work [13,18,19].

Table 1.1. Electrochemical performance metrics

Measured metrics		
Voltage (V) – V	Current (i) - mA	
Time (t) – h	Area (S) - cm^2	
Calculated metrics	**Equations**	**Units**
Capacity (C)	$C = i \cdot t$	mAh
Current density (j)	$j = i / S$	mA/cm^2
Areal capacity (C_A)	$C_A = i \cdot t / S$	mAh/cm^2
Specific capacity (C_g)	$C_g = i \cdot t / m$	mAh/g
Gravimetric energy density (E_g)	$E_g = I \cdot V \cdot t / m$	Wh/kg
Coulombic efficiency (CE)	$CE = C_{(discharge)} / C_{(charge)} \cdot 100$	%

The exchange current density is a measure of the electron-transfer activity at the equilibrium potential [5]. High exchange current density indicates that significant oxidation and reduction reactions occur, whereas a low value reflects the opposite [12]. At Li deposition, the exchange current density can provide information to understand the electron-transfer activity on the electrode to reduce Li-ions to metallic Li [5]. The current density at equilibrium is expressed as [5]:

$$j_0 = j_a - j_c \qquad (1.5.)$$

where j_a and j_c are the partial anodic, and cathodic current densities, respectively, and the magnitude of these partial current densities at equilibrium is known as the exchange current density [5]. Practically, the exchange current density can be determined from so called Tafel plots where the logarithm of current vs voltage is plotted and the current is then extrapolated to the

point of zero voltage as shown in Fig. 1.4. [5]. In the work of Y. Liu *et al.* with the help of phase-field modelling and experimental characterization it was concluded that the lower exchange current density is, the larger the radius of nucleis form and therefore it is directly related to the uniforming at deposition of Li-metal [5].

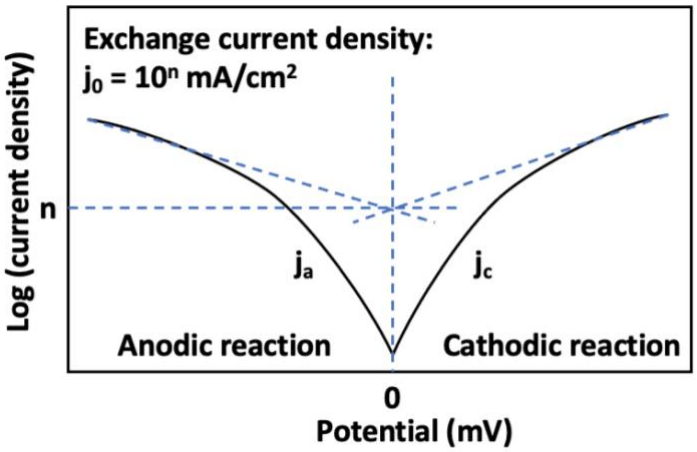

Fig. 1.4. Tafel plot for exchange current density determination [5]

1.3. Li-ion batteries

It's been 30 years since Sony commercialised the first LIB system with a $LiCoO_2$ cathode and a graphite anode, and it is still the most successful solution for efficient electrochemical energy storage [17,20]. In 2019, J.B. Goodenough, M.S. Whittingham, and A. Yoshino received the Nobel prize for their work on the electrochemical intercalation concept followed by studies of the different electrode materials. Safety issues that arose with the utilization of lithium metal as anode material (which was the preliminary idea in the 1970s [21]) were solved by utilizing graphite [3,22].

The base of a graphite anode cell is that, once it is assembled, it is in a discharged state, with Li-ions in the cathode. When current is applied, Li-ions are transferred to the anode and intercalated between graphite layers (Fig. 1.5.) [23]; hence the cell is being charged. Respective reduction and oxidation reactions occurring during charging are [14]:

$$LiCoO_2 \rightarrow Li^+ + e^- \quad (1.6.)$$

$$C_6 + Li^+ + e^- \rightarrow C_6Li \quad (1.7.)$$

During discharge, Li-ions travel back to the cathode, releasing electrons to the external circuit to provide energy [23].

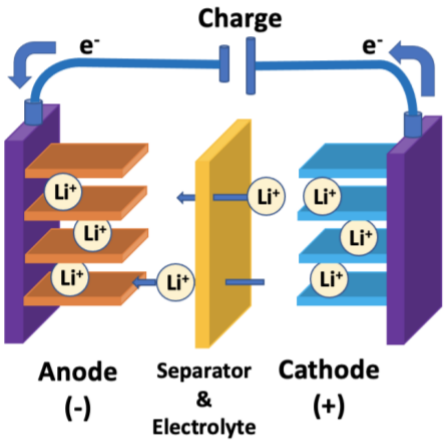

Fig. 1.5. Li-ion battery working principle during charge [23]

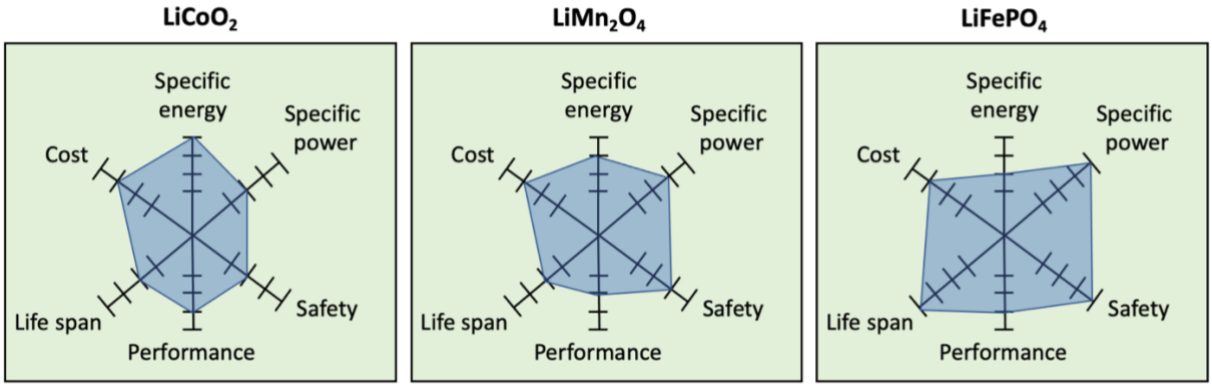

Fig. 1.6. Comparison between properties of commonly used cathode materials [24]

A large variety of materials can be used as a cathode for LIBs, such as the already mentioned $LiCoO_2$, $LiFePO_4$, different layered oxides, spinel oxides [25], and many more. Fig. 1.6. presents an evaluation of some properties for the most commonly used cathode materials. $LiCoO_2$ was used in the first commercial LIB; however, it has a relatively short cycle life, low specific power, and there are concerns about safety [20,24]. $LiMn_2O_4$ has a higher specific power (power per material weight) and safety; however, it is less thermally stable and has a lower specific energy. $LiFePO_4$ possess the highest safety, life span and specific power of the compared cathode materials but a significant is lower specific energy [24].

The most used anode material is graphite with a theoretical specific capacity of 372 mAh/g. Silicon is another proposed material for the anode with a very high capacity (4200 mAh/g), but it has significant volume expansion during lithiation (charging process) which can cause failure [26]. Hence, depending on the anode and cathode used for a battery, the properties may change, and it is upon the manufacturer to decide what are the most important parameters to consider for a particular system [24]. Another vital consideration that must be taken into account is that in practice a battery does not consist only of active materials that provide energy. Fig. 1.7. shows how gravimetric and volumetric energy decrease gradually by an increase in scale from material to cell to pack [3].

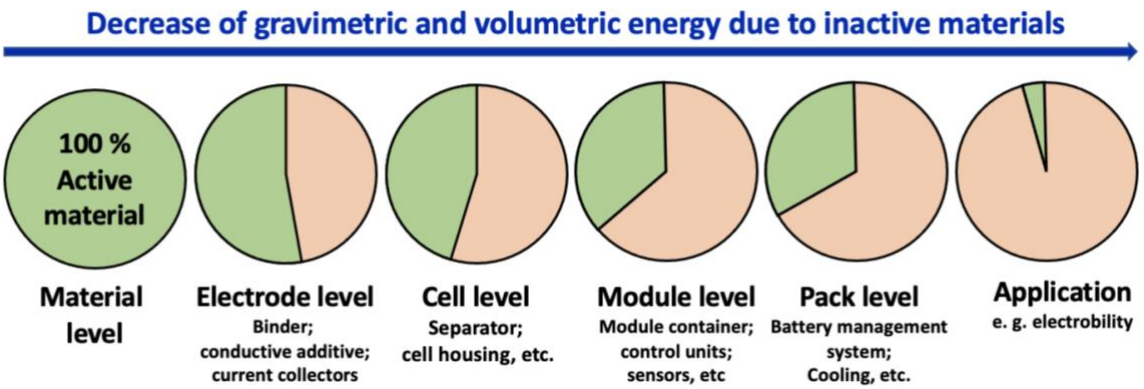

Fig. 1.7. Energy decrease by moving to large scales [3]

Even though it is hard to predict the availability of materials, one of the factors to consider as well is raw material abundance since it is closely related to the material costs. As there are concerns of, for instance, cobalt and nickel depletion, researchers are considering other constituent materials and strategies [3]. Fig. 1.8. is an overview of element suitability for battery systems. Elements coloured in yellow, blue pink and violet are excluded due to toxicity, radioactivity, weight and costs. In contrast, in green are highly preferred elements as electrode materials; in fact, those in pale green could still be considered [3].

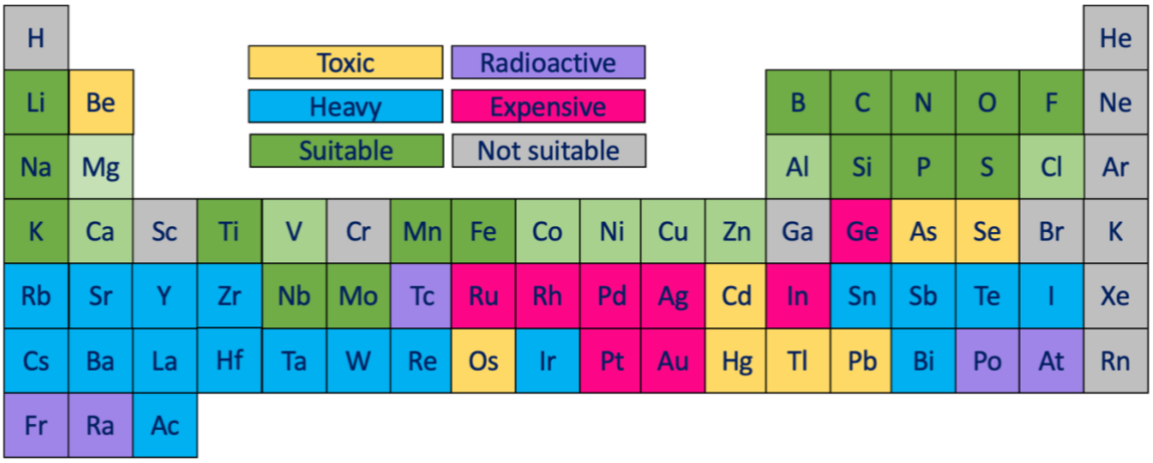

Fig. 1.8. Evaluation of element suitability as electrode materials [3]

1.4. Li-metal batteries

Since the 1970s, Li-metal has been considered as "holy grail" anode material because of its ultrahigh theoretical specific capacity, 3860 mAh/g, low reduction potential of -3.04 V vs SHE (providing higher overall voltage within the cell), and low density of 0.534 g/cm^3 [27]. However, it is very challenging to develop Li-metal batteries due to a low coulombic efficiency (CE) and severe safety hazards [6]. However, reaching the limits of energy density that the Li-ion strategy can provide, there are now several initiatives to implement Li-metal in battery systems [6], which could potentially double the energy density compared to current Li-ion batteries [14].

When using Li-metal, the cell chemistry is changed, and stripping and plating on the anode are introduced:

$$\text{Stripping: } Li \rightarrow Li^+ + e- \quad (1.8.)$$

$$\text{Plating: } Li^+ + e^- \rightarrow Li \quad (1.9.)$$

During discharge, lithium is being stripped off the anode, and the Li-atom is split into a Li-ion and an electron, whereas during charge, a Li-ion is combined with an electron; and a Li atom is formed and plated back on the anode. Fig. 1.9. shows a schematic of the electrodeposition process of Li-metal. Repetitive plating provides problems that hinder Li-metal utilization as anode material [5,28]. The main challenge is that during electrodeposition, Li-metal plates in an irregular manner, forming spike-like microstructures (dendrites) causing low CE and safety issues which will be explained more in-depth in the chapter about challenges [14].

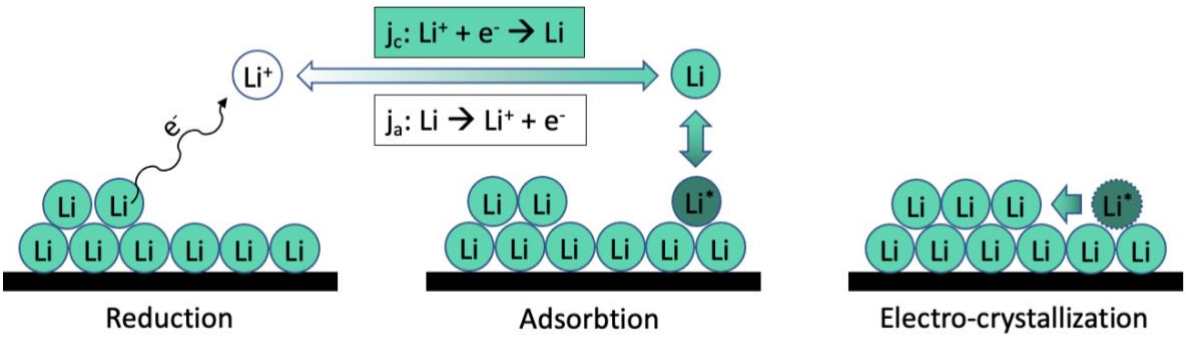

Fig. 1.9. Schematic of electrodeposition of Li-metal [5]

Currently, the most studied NGBs that use Li-metal as an anode are Li-S, Li-O_2, and solid-state batteries. The main idea in Li-S batteries is that during discharge, sulfur is reduced

to lithium sulfide through different polysulphide species. Even though sulfur is a very inexpensive and abundant material, such systems have several drawbacks apart from dendrite growth and low CE – low conductivity at active material and shuttle reactions [1,10]. Li-O_2 batteries, also known as Li-air batteries, are promising due to material abundance and very large theoretical specific capacity. However, for commercialization, the power and life-cycle of such a system require significant improvements [1]. Solid-state batteries would provide much safer batteries because of utilizing a solid electrolyte instead of flammable liquid. Their current disadvantage is high cost and, it is also challenging to ensure good electrode contact during cycling with short cycle life as a result [1].

1.5. Challenges

The low CE and safety hazards of Li-metal batteries are mainly caused by dendrite formation during the charging process. Many efforts have been devoted to explain the electrochemical mechanisms behind this uneven deposition [28–30]. It is recognized that dendrite formation is dependent on many different complicated, simultaneously occurring, processes. One important process is mass transport that describes the movement of species [6]. There are 3 types of mass transport: diffusion, migration, and convection. During charge, Li-ions move from the bulk electrolyte close to the electrode and adsorb on its surface and are reduced and diffuse on the surface to be incorporated within the metal lattice. These processes, to a large extent, determine the final morphology of electroplated lithium [6].

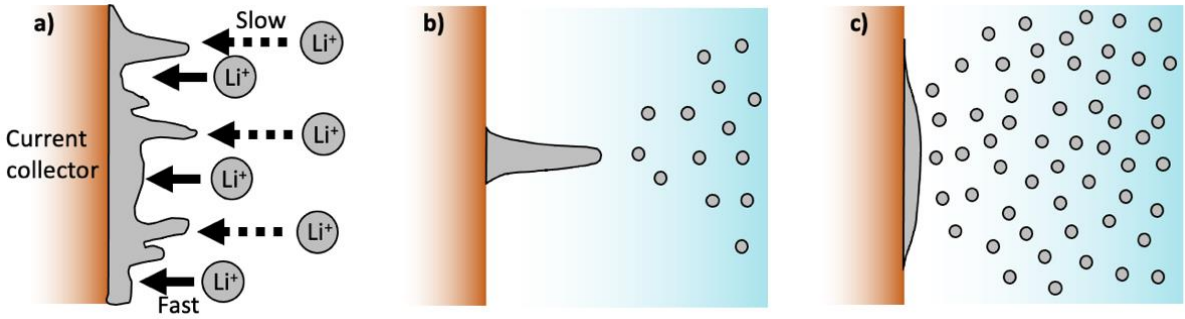

Fig. 1.10. Dendrite formation (a) and dependence on ion concentration within electrolyte – low concentration (b), high concentration (c) [28]

As illustrated in Fig. 1.10. a low concentrations of Li ions in the electrolyte causes uneven ion distribution, and ions tend to deposit on nearest available nucleation centre, thus forming dendrites. Continuous dendrite growth can cause penetration through the separator, leading to an internal short-circuit. Higher Li-ion concentration (Fig. 1.10. c) leads to more even plating because of the smaller concentration gradient near the interface. Thus, one way to increase uniform deposition is to decrease the mass transport effect, providing a more even distribution of ions near the electrolyte/anode interface [28]. Another problem with dendrites is their fragility. At repetitive discharge/charge, they might break introducing inactive "dead" lithium on the anode as these fragments become disconnected from the electrical circuit. That leads to rapid capacity fading and low CE [28].

Most organic solvents are thermodynamically unstable towards lithium and when it is immersed in an electrolyte, a solid electrolyte interphase (SEI) is formed [8,28,31]. The SEI consists of insoluble and partially soluble products of electrolyte decomposition [31]. Fig. 1.11. illustrates the voltage stability window of an electrolyte. It represents the potential interval (a

grey area) in which the electrolyte is stable and would not initiate side reactions. Outside the grey area, the electrolyte would react providing an SEI [20].

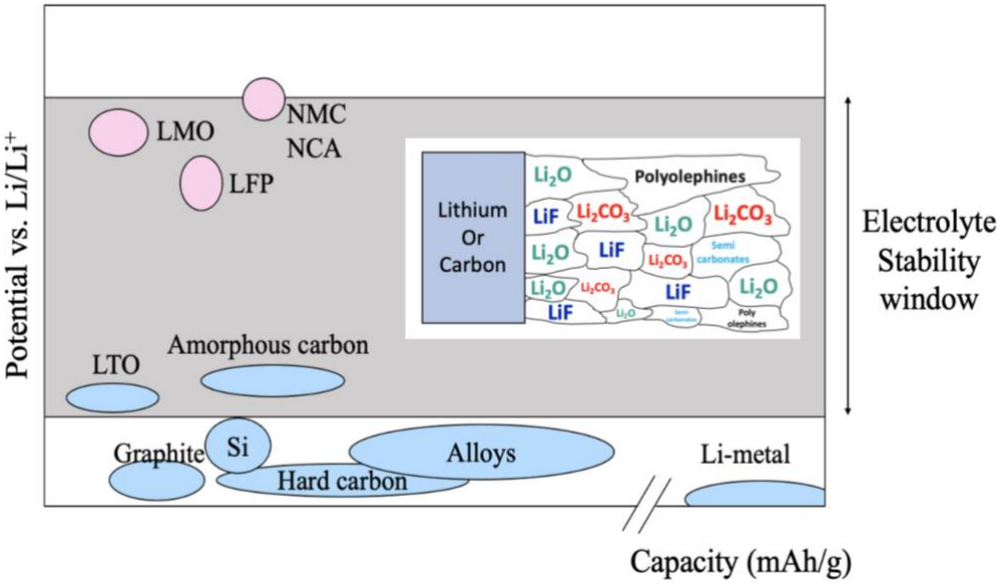

Fig. 1.11. Electrolyte stability window [20] (inset – SEI products formed from Li-metal and electrolyte components [31])

In Fig. 1.11. some of SEI products are illustrated. It is beneficial to have an SEI with a high electrical resistance, the thickness of few nanometres, high mechanical strength and flexibility, insolubility in the electrolyte and thermal stability. However, usually, the SEI does not have all of these properties, and it sometimes continues to grow over discharge and charge cycles [31]. When Li-metal participates in reactions to form an SEI, it is consumed irreversibly and cannot participate in plating and stripping [8].

1.6. Strategies to overcome challenges

Many efforts have been made to increase the coulombic efficiency during cycling and achieve uniform morphology of Li deposits [17,32]. One of the widely studied methods is the adjustment of the electrolyte composition. Usually, the electrolyte consists of a solvent or solvent mixture and a Li salt. It is common to add small amounts of additives to improve reversibility and stability. The most common solvents are nonaqueous aprotic solvents, such as alkyl carbonates and ether compounds, because of their relatively high electrochemical stability voltage window [33].

H. Jin et al., has shown that the performance of Li-metal cells improves with the addition of $LiNO_3$ and that with increased concentration of $LiNO_3$ the cell can run longer without short-circuiting and with higher CE. Field Emission Scanning Electron Microscopy (FESEM) images also show that uniform Li deposition was obtained. However, why and how the addition of $LiNO_3$ makes so big of a difference is still unclear, but it is speculated that it preferentially reacts with Li metal, before the solvent and the Li salt, and therefore a better SEI is formed [8,33]. In this thesis, the electrolyte composition was a mixture of 1,3-dioxolane and 1,2-dimethoxyethane (DOL: DME (1:1v)), 1 M lithium bis(trifluoromethane sulfonyl)imide (LiTFSI) and $LiNO_3$ as additive. This is a very commonly used electrolyte formulation that provides promising performance with a CE reported to reach up to 99.1 % [8,17,34].

Another strategy to suppress dendrite growth is providing an artificial SEI by covering the Li surface with a protective layer before cycling. This layer should be mechanically robust towards dendrite propagation. Some chemicals used to provide this artificial SEI are tetraethoxysilane-generated silicate, N_2 (providing Li_3N coating at room temperature), and acetylene to form polyacetylene through *in situ* polymerization [6].

To ensure even Li-ion distribution on the electrode surface and uniform plating, a strategy is to increase the effective surface area of the electrode. This is achieved by designing a nanoarchitecture of a metal current collector, for example, 3D Cu current collector. Numerous perturbances within the 3D structure may act as nucleation sites, providing a more uniformly distributed electric field and stable CE, reaching 98.5 % [6,35]. Another route is to use rapid voltage pulses (of - 5 V to 5 V amplitude) as a pre-treatment to achieve uniform lithium deposition. However, here the coulombic efficiency is not reported, which is an essential performance parameter [32].

1.7. Characterization methods for morphology studies

To move a step forward to the unveil lithium electrodeposition mechanisms, one must consider the characterization methods available. There are various ways to characterize a cell. First of all, it is essential to introduce approaches commonly used in literature – *ex situ* [18], *in situ* [23,32] and *operando* [11,36] (Fig. 1.12.). *Ex situ* measurements refer to the study of individual cell components. *In situ* studies stand for characterization of materials or components of the cell in an assembled state without making any changes to the environment [23]. *Operando* studies mean that the cell is studied while it is in operation, being cycled [11,36].

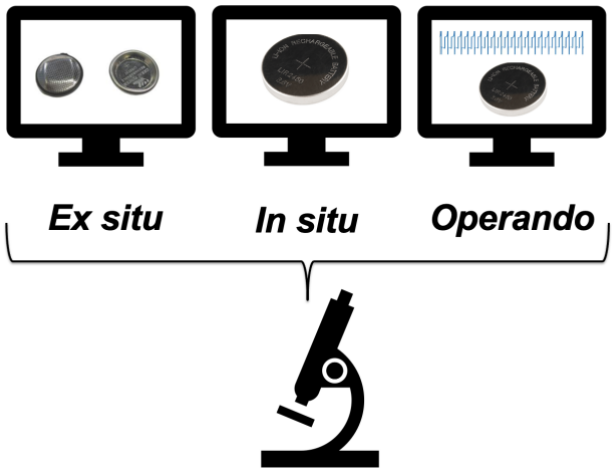

Fig. 1.12. Comparison between *ex situ*, *in situ* and *operando* approaches

There are countless methods to study electrochemical deposition mechanisms and, each has its advantages and disadvantages. Examples are Optical Microscopy [32], Scanning Electron Microscopy (SEM) [13], Transmission Electron Microscopy (TEM) [6,37], X-ray Tomography [10] and Gas-Chromatography [30]. All methods provide different resolution in what intervals we can study our sample. Also, complexity in the set-up and opportunities the technique offers by investigating processes while the electrochemical measurement is occurring are different. The disadvantage of microscopy techniques is that there are limits on how big area in the cell that can be covered and measured. In 2D techniques, the information in-depth cannot be observed, but they are faster than 3D techniques. X-ray Tomography allows to scan relatively large areas in a cell [6,10]; that is why this method is chosen to study electrochemical mechanisms within this thesis.

In a report by Kevin N.Wood et al. [36], dendrite growth is studied with *Operando* Video Microscopy. Measurements were acquired continuously, giving a good insight into the process

during battery operation. It was possible to correlate obtained voltage profiles with the evolution of the morphology. However, this kind of observations are two-dimensional, and they cannot be quantified across the entire active area. C.Tan et al. studied Li-S batteries by X-ray Tomography imaging [29]. The principle was to do galvanostatic measurements and simultaneous tomographic imaging. Every 15 minutes, cycling was stopped, and the image was taken. However, pausing the current may allow the system to relax, consequently introducing changes within the system, but it was still possible to follow process and in 3D observe microstructural evolution during discharge and charge with quantification of the solid sulfur phase within the cathode [10].

1.8. X-Ray Tomography Microscopy

X-ray Computed Tomography is a non-destructive imaging technique where individual X-ray images recorded from different angles are used to reconstruct the object's internal structure with high spatial resolution, Fig. 1.13. [38,39].

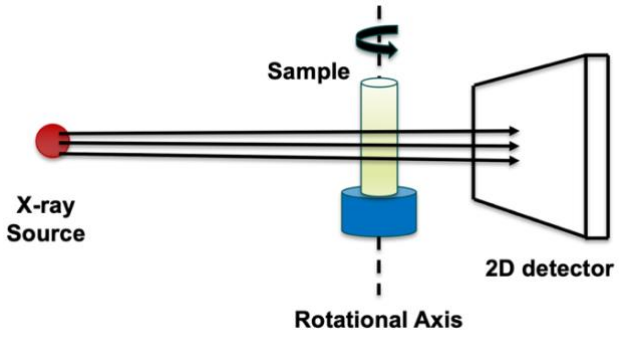

Fig. 1.13. Illustration of the principle of CT Imaging [39]

The sample is placed on a rotary stage between the X-ray source and the detector and is then rotated through 180º. X-rays propagate through the sample, some of them are absorbed, and the intensity of the transmitted X-rays is measured, based on Beer-Lambert law. The transmitted X-rays pass through a scintillator where they are converted to near visible light, and which is then measured by a 2D charge coupled device detector. The detector produces a greyscale image showing contrast between phases with differing absorptions. The signal on the detector can be correlated with the electron density distribution in the sample and can be represented as a greyscale 2D pixel map. Finally, image processing is used to reconstruct, visualise and analyse the obtained data [38,39].

Three parameters to consider during data acquisition are the area to be imaged, field of view and acquisition time. The area that can be imaged at once is dependent on the detector and is known as detector area coverage. It will determine how many sets of images are required to image the whole area of interest from the object. The field of view is the maximum diameter of the area represented in the reconstructed image. The time of data acquisition will determine how fast data can be captured and how often measurements can be done [38].

2. MATERIALS AND METHODS

2.1. Electrolyte preparation

To study the performance of Li-Cu cells and the morphology of Li deposits, electrolytes with various concentrations of $LiNO_3$ (Sigma Aldrich, 99.9 %) additive (0 M, 0.1 M, 0.25 M, and 0.5 M) and 1 M LiTFSI (Solvionic, 99.9 %, extra dry < 20 ppm water) in mixture of 1,3-dioxolane (DOL) (Sigma Aldrich, anhydrous, 99.8 %, contains ~75 ppm BHT as inhibitor) and 1,2-dimethoxyethane (DME) (Sigma Aldrich, anhydrous, 99.5 %, inhibitor-free) (1:1v) were prepared. DOL and DME solvents were kept overnight in a vial with zeolites to reduce water content. Electrolyte solutions were prepared in a glovebox filled with argon to ensure the absence of oxygen and water as all the materials are very water and air-sensitive.

2.2. Coin-cell assembly

Li-Cu coin-cells were assembled in an argon-filled glove box. 13 mm diameter Cu foil (Goodfellow, 99.95%) discs were cut and washed with acetone and 2-propanol in an ultrasonic bath (15 minutes in each) and then dried in vacuum for 2 hours at 60°C. Celgard 2400 separators were cut in 16 mm diameter discs and dried in vacuum for 2 hours at 40°C. The rest of the coin cell components – cases, lids, gaskets, springs, and spacers were dried overnight at 70°C. Li (source and purity unknown) discs (14 mm) were punched in the glove box. Fig. 2.1. a) shows a coin-cell set-up and order of components, and in b) shows assembled coin cells. The separator was soaked with 20 μL of electrolyte.

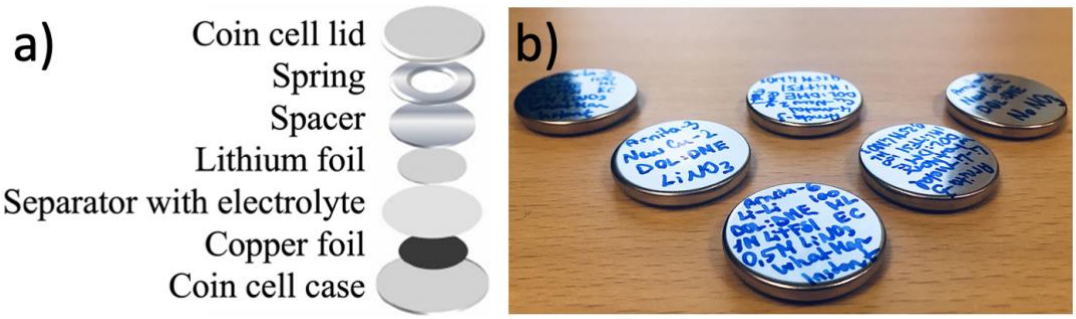

Fig. 2.1. a) Coin cell components [40]; b) Assembled coin cells

2.3. Electrochemical measurements

2.3.1. Stability tests

To determine the electrochemical performance of the assembled coin cells, they were galvanostatically cycled using a Scribner 580 battery test system, with a current density of 0.1 mA/cm^2. The intention was to run the cells until they short-circuit, in other words, until failure (Fig. 2.2.). For safety reasons, the cut-off voltage limits were set to: -2 V for discharge and 1.5 V for charge to prevent stripping of copper.

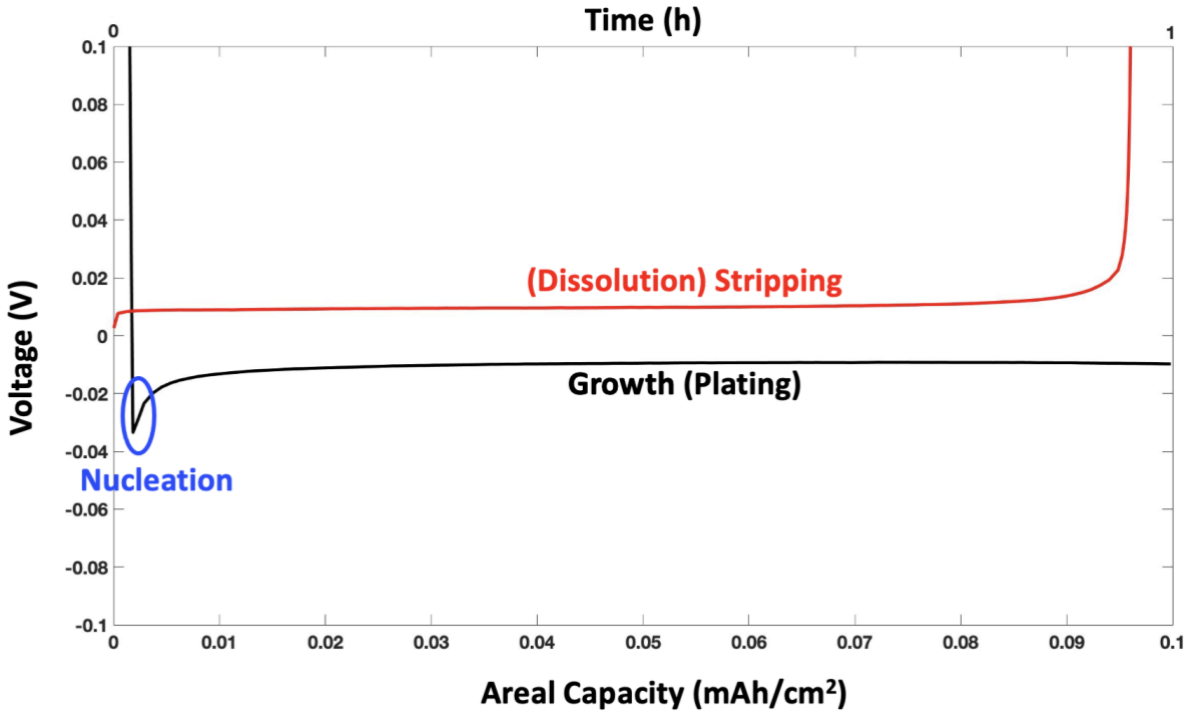

Fig. 2.2. Galvanostatic cycling data for a cell with 0.5 M $LiNO_3$ in electrolyte

The coulombic efficiency for each cycle was calculated. In the introduction section, CE was explained as a ratio of discharge and charge capacity. In fact, that applies to the cell configuration where Cu is the anode material. Within this thesis the deposition process of lithium is studied by plating/stripping it on a Cu substrate by building a Li-Cu cells where Li is anode material and Cu is cathode as there reduction takes place during discharge. Thus, we start with discharge (plating) and measure the ratio of the stripped lithium to the plated lithium on copper. Another property that could be determined and is shown in Fig. 2.2. is the nucleation potential, i.e. the potential required to initiate lithium growth on copper. Even though various processes contribute to the overpotential, as explained section 1.2, the nucleation potential was determined by the minimum potential value during plating.

2.3.2. Rate tests

Rate tests were performed to observe coin cell cycling capability at different applied current densities. This relates to the speed at which a battery could be charged or discharged. First coin cell, set-up with one Celgard separator, did not work well and the cell was short-circuited (SC) very soon when cycled at 2 mA/cm^2. One approach to increase the distance between electrodes, thus lowering the chances for SC, was to use a Whatman glass fiber separator sandwiched between two Celgard separators and increase the amount of electrolyte by 5 times (100 μL). The applied rate program for cycling was also modified to a gradual increase in the applied current density – 0.1 mA/cm^2, 0.2 mA/cm^2, 0.5 mA/cm^2, 1 mA/cm^2 and 2 mA/cm^2 with cycle times of 1 hour, 30 min, 12 min, 6 min, and 3 min, respectively.

2.3.3. Pre-deposition tests

Electrochemical stability was also studied for coin cells where 0.1 mAh/cm^2 of Li was initially deposited. Further cycling was applied by continuous discharge and charge, as previously explained for stability tests.

2.3.4. Exchange current determination

To determine the exchange current density, symmetric Li-Li cells were assembled. For these measurements, 13 mm diameter Li discs were used and a 16 mm diameter Whatman glass fiber separator soaked with 100 μL electrolyte (DOL: DME 1 M LiTFSI with 0 M $LiNO_3$ and 0.25 M $LiNO_3$). Cells were tested in two ways. They were measured instantly after assembly or pre-cycled (25 cycles with a current density of 0.1 mA/cm^2). The approximate number of cycles for SEI formation were determined by stability tests.

2.4. *Operando* X-ray Tomography imaging

To perform *operando* Tomography imaging of Li-Cu cells, the cell set-up was adjusted to meet the experimental requirements. The *operando* cell used in the experiments is shown in Fig. 2.3. It consists of a stainless-steel pin with Li metal on top and a copper pin on the bottom, surrounded by X-ray transparent polyetheretherketone (PEEK) tubing. The pin electrodes were 1.58 mm in diameter with a fixed 1 mm distance between them. X-ray Tomography experiments were performed at the Swiss Light Source at Paul Scherer Institute (PSI) at the TOMCAT Beamline. For the measurements, a monochromatic beam, 18 keV, was used.

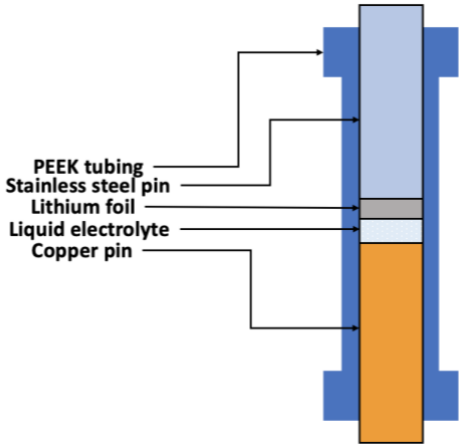

Fig. 2.3. Cross-section of the *operando* cell used for X-ray tomography

To study morphology of deposited lithium during cell cycling, the *operando* cell was connected to a potentiostat and cycled at 0.5 mA/cm^2. X-ray tomographic images (projections) were captured before cycling and after cycling. In this thesis, results for 0 M and 0.25 M $LiNO_3$ within the electrolyte will be presented. The general workflow scheme from data acquisition until obtained results is shown in Fig. 2.4. At each measurement 1000 projections were acquired (total acquisition time 50 s) and reconstructed to obtain tomogram slices. The whole set of stacked slices gives information of the entire 3D volume. The most time-consuming step is to process and analyse the data, where the main step is segmentation, during which the lithium volume is selected from the whole volume and rendered to binary images from which lithium morphology can be quantified. The data processing and segmentation workflow adjusted for this particular project is shown in Fig. 2.5.

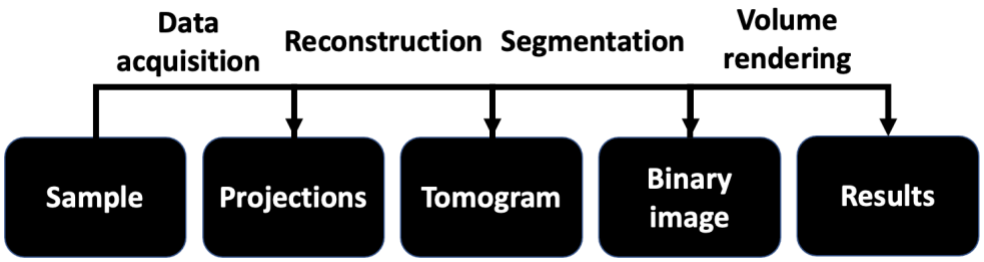

Fig. 2.4. Tomography imaging workflow

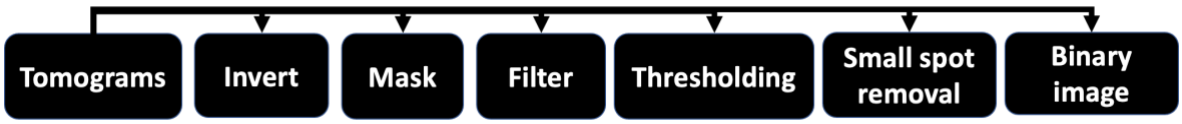

Fig. 2.5. Tomography image processing workflow in Avizo program

Data processing was done using the software Avizo. As the X-ray Tomography imaging technique perceives information about the sample by considering X-ray absorption, there is a requirement for a sample to have differences in electron density to distinguish one phase from another. Lithium is a very light element with low electron density, and it is assumed to be almost X-ray transparent. As the used electrolyte consists of elements with higher electron density, it was still possible to distinguish lithium from the electrolyte. As lithium is almost X-ray transparent and in tomograms appeared as "gaps," obtained tomogram images were inverted for user convenience, where light areas are Li.

As data were acquired, even though the shape of the interest was circular, images were obtained in square shape. That was because of the square detector geometry. However, data in the corners are not collected for all angles. Therefore, data from the corners were removed (cropped) and images were masked to retain on the field of view.

To remove any background noise and obtain higher resolution, different filters were applied. To assess which filter to use, it was necessary to determine the resolution of the filter. Resolution determination was done in ImageJ software with the help of the following method. A certain area of interest was chosen within a particular slice, which included a dendrite surrounded by electrolyte. For that area, every filter was applied with two different provided settings, either 2D or 3D. When the image was opened in ImageJ software, three different coordinates were chosen to determine resolution. These coordinates were chosen for areas within the image with the highest visual contrast difference, i. e. the highest observable difference in greyscale, practically – the edges of the dendrites and electrolyte. The scale was

set so that 1 px is 0.325 µm. When certain coordinates at high contrast area were selected, the plot was obtained that is shown in Fig. 2.6. In this plot, minimum and maximum values were determined of the greyscale, and then for the difference of these values, 5 %, and 95 % were calculated and found the intercept on the x-axis between them, which gives a resolution.

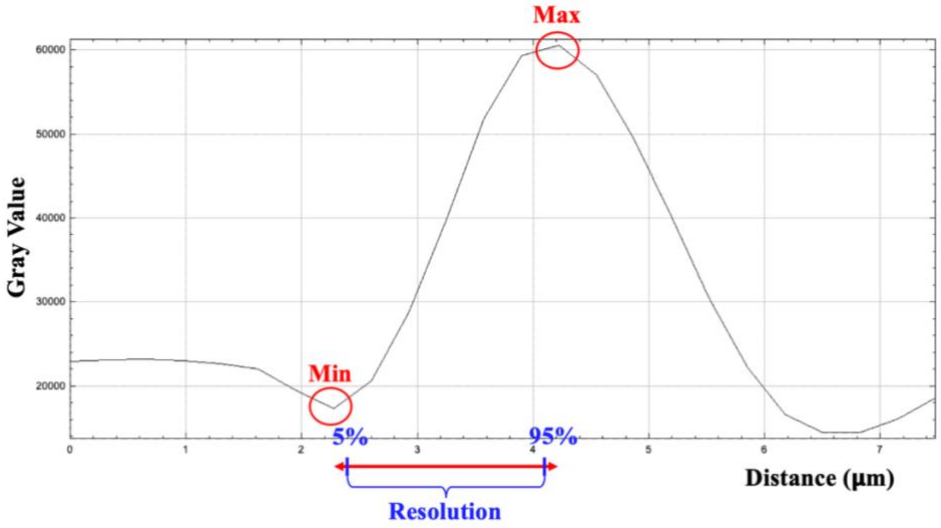

Fig. 2.6. Determination of resolution

After application of the filter segmentation follows. It is a crucial step during which the aim is to extract sub-volumes that represent only lithium metal. Within software this was done by using the command "Interactive Thresholding". This command requires setting a greyscale value, which corresponds to interface between the electrolyte and lithium. Thus, distinguishing is possible because of the difference in electron densities of the two materials. Since each greyscale value corresponds to a particular electron density. It is essential to find the appropriate threshold value. If the threshold value is set too low, background noise is selected; however, if the threshold value is too high, information is lost. To choose the threshold values as precisely as possible, label analysis was done within the software. Label analysis is a command that helps to identify the amount of individual objects as a specific threshold value is applied. Additionally, the "Small spot removal" command was used to remove minimal extra background noise. That was done by setting a certain threshold for the pixel area under which all the smaller pixels (voxels) were removed. Appropriate settings were decided by variation of threshold values, removing small spot value, and checking how many separate objects there were. After segmentation, binary images with only lithium could be exported. And from binary images, precise quantitative values of voxel amount could be obtained, representing the volume of lithium deposits.

3. RESULTS AND DISCUSSION

3.1. Electrochemical measurements

3.1.1. Stability tests

The first discharge and charge cycles for cells with various concentrations of $LiNO_3$ in the electrolyte are shown in Fig. 3.1. The voltage profiles were obtained during galvanostatic cycling with a current density of 0.1 mAh/cm^2.

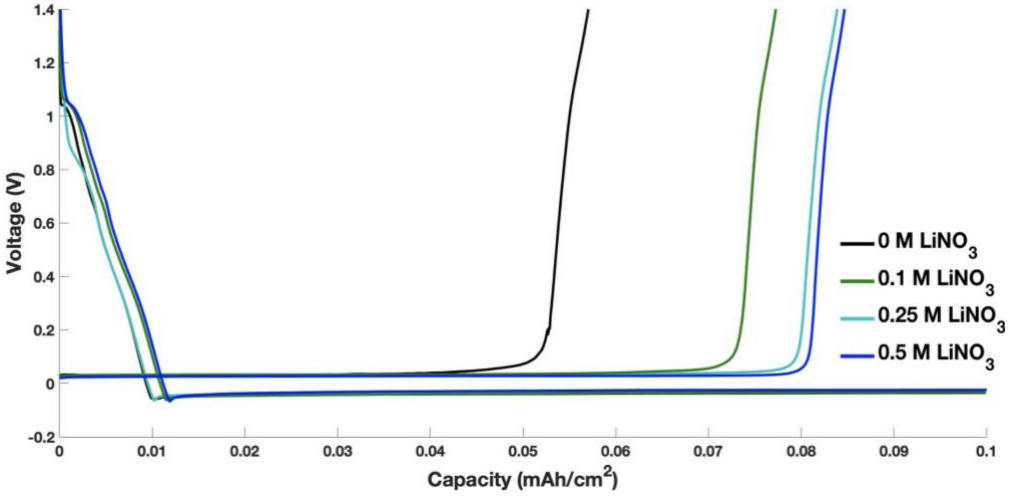

Fig. 3.1. First cycle voltage profiles from cells with various lithium nitrate concentrations in the electrolyte

The curves, starting from a voltage value of 1.4 V, visualise the discharge process, plating of lithium. 1 hour of plating gives 0.1 mAh/cm^2 of plated lithium. The rapid decrease in potential until 0.01 mAh/cm^2 of capacity is related to plating of lithium on copper and formation of SEI [19]. The overvoltage minimums correspond to the nucleation potential, which is related to the excess energy required to nucleate lithium on copper [13]. After one hour of discharge, the current is reversed, and now the charge process takes place, stripping the lithium from the copper. The rapid voltage increase (Fig. 3.1.) means that all lithium that can be stripped of the copper has been removed. There is a significant difference between the samples with and without lithium nitrate added to the electrolyte. When lithium nitrate is added, the retrieved amount of lithium varies from ~ 0.07 - 0.08 mAh/cm^2. However, for the cell of 0 M lithium nitrate, retrieved capacity was only half of the introduced one. The importance of added $LiNO_3$ could be explained by the nature of the SEI [8].

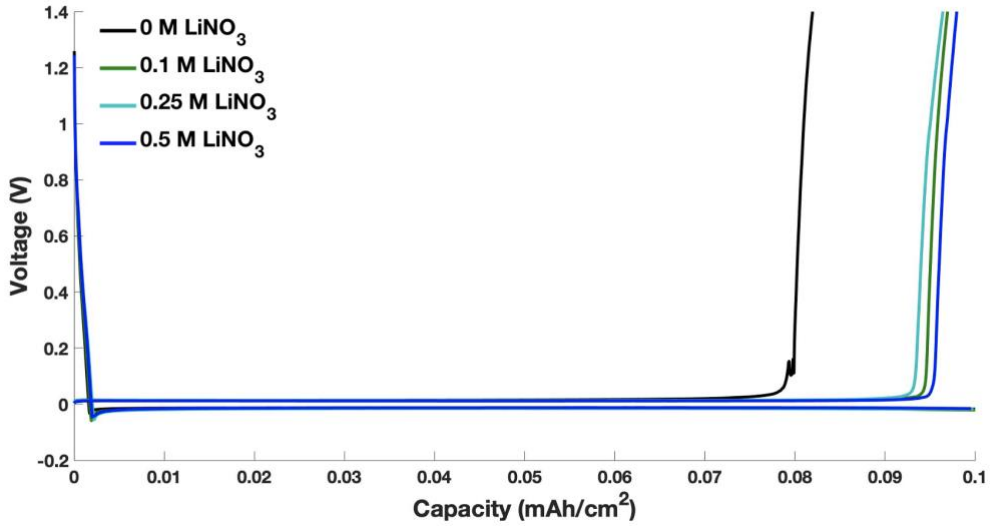

Fig. 3.2. 20th cycle voltage profiles from cells with various lithium nitrate concentrations within the electrolyte

Fig. 3.2. shows the 20th cycle of discharge and charge for cells with the different $LiNO_3$ concentrations in the electrolyte. For all cells with and without lithium nitrate, retrievable capacity has increased compared to the first cycle, however, it is still lower for the cell without $LiNO_3$.

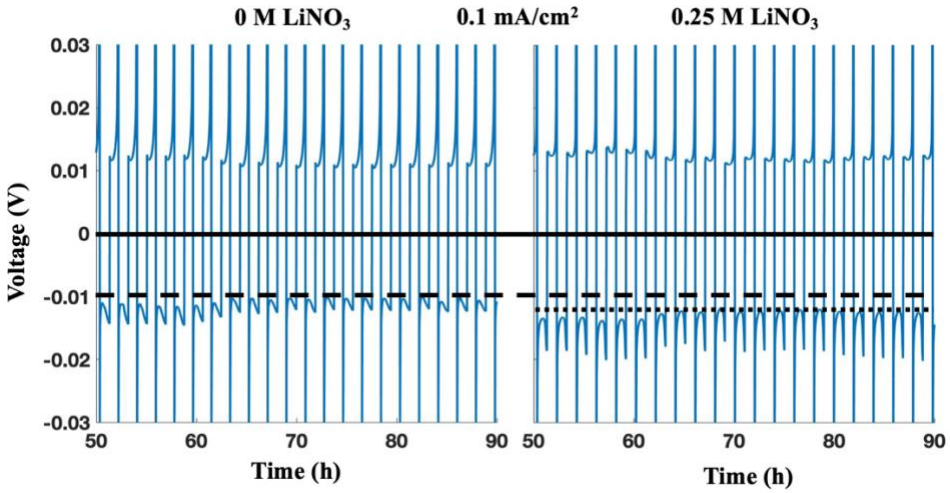

Fig. 3.3. Voltage profiles from cells without and 0.25 M $LiNO_3$ in the electrolytes

In Supplements 1-4, the full voltage profiles of the cells are presented, whereas in Fig. 3.3., voltage profiles in the time interval 50 – 90 h are shown. From the figure it is clear that by that time the system has stabilized, i.e., it has a stable overpotential. In the cell without lithium nitrate, the overpotential is lower than in the cell with lithium nitrate. That could mean

that due to the nature of the formed SEI, more energy for Li-ions to diffuse through the SEI is required when $LiNO_3$ is added, but also other processes, e.g., the viscosity of the electrolyte, should be considered [41].

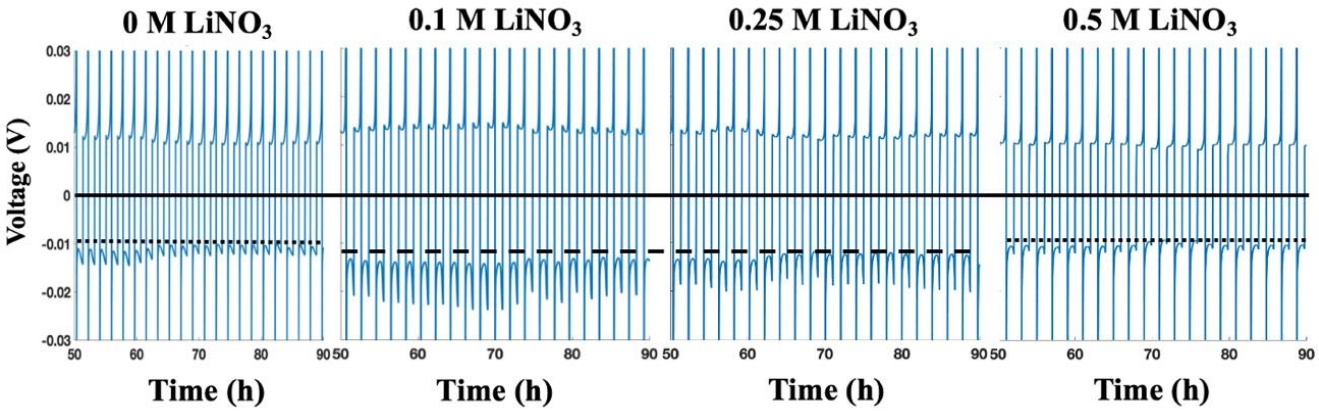

Fig. 3.4. Voltage profiles of cells with 0 M, 0.1 M, 0.25 M, and 0.5 M $LiNO_3$ added to the electrolytes

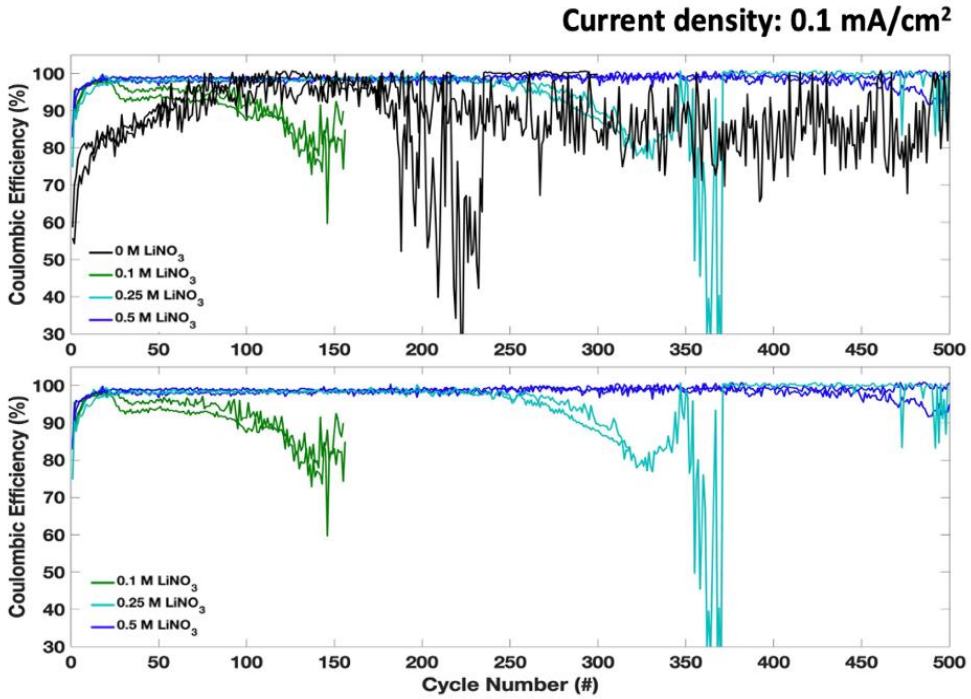

Fig. 3.5. Coulombic efficiency of the cells with various $LiNO_3$ concentrations in the electrolyte

In Fig. 3.5., the coulombic efficiency of the cells with different $LiNO_3$ concentration in the electrolyte is presented. Cells without lithium nitrate show low and unstable CE ~ 80 % on

average. By adding 0.1 M of lithium nitrate, the CE increases rapidly; however, after 20 cycles it decreases and eventually the cell short circuits around 150 cycles. That might be explained by a depletion of lithium nitrate, that it is consumed in a continuous SEI formation. When the lithium nitrate concentration is increased to 0.25 M, the cycling is stable with an average CE of 98-99 %. After 300 cycles, the CE decreases rapidly and then the cell short circuits. Finally, the 0.5 M $LiNO_3$ cell shows stable cycling for at least 500 cycles without short-circuiting and a CE of ~ 99 %. These results point to that lithium nitrate is consumed during cycling.

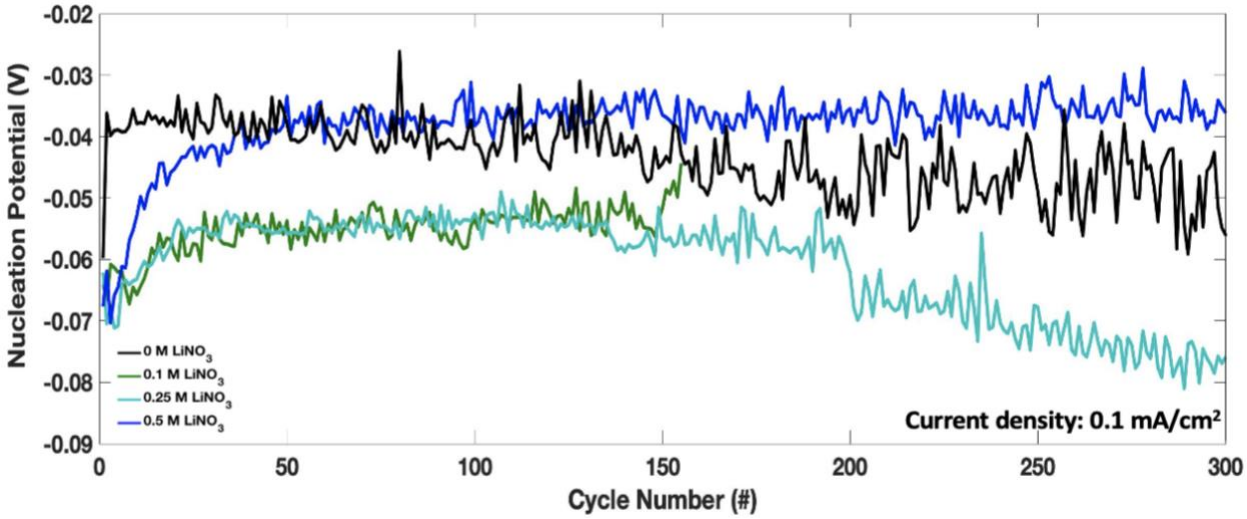

Fig. 3.6. Nucleation potential as a function of cycling for the cells of various $LiNO_3$ concentrations in electrolyte

Figure 3.6. shows the nucleation potential as a function of cycling. The nucleation potential for cells without $LiNO_3$ is low at first but slowly increases during cycling. With a low amount of lithium nitrate in the cell (0.1 and 0.25 M) the nucleation potential is higher and relatively stable. With a high amount of $LiNO_3$ (0.5 M) a low nucleation potential is observed, and it remains stable through all cycles.

3.1.2. Rate tests

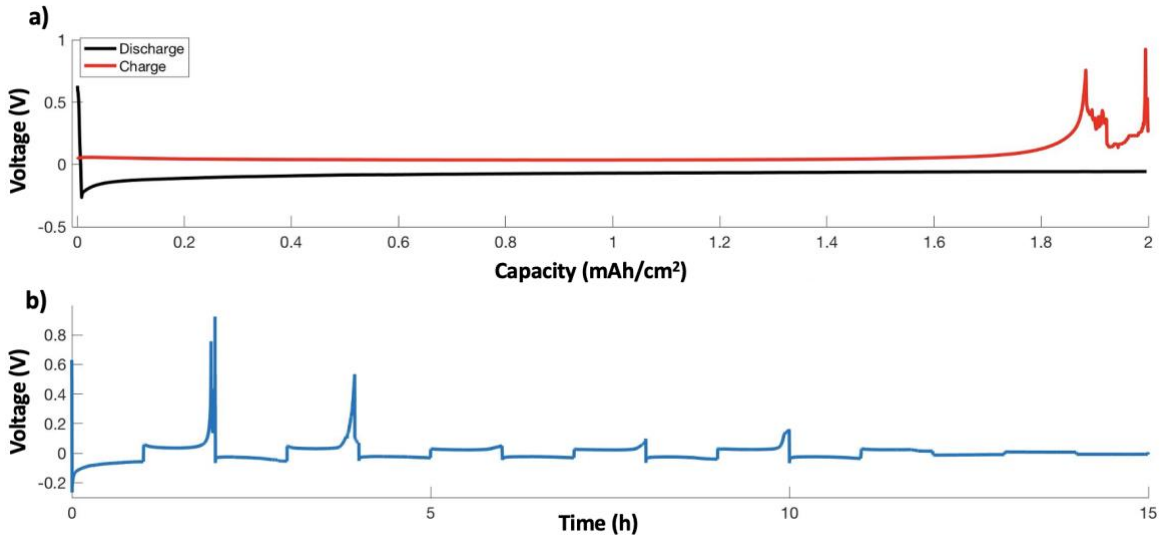

Fig. 3.7. Rate tests of the cell with 0.25 M $LiNO_3$ in the electrolyte with a single Celgard set-up a) First cycle b) Full voltage profile

The first attempt to run 0.25 M $LiNO_3$ cell at 2 mA/cm^2 is shown in Fig.3.7. The same cell set-up was used for this test as in the stability tests (one Celgard 2400 separator). The first discharge was successful, but the cell went to soft short circuit during the first charge. A soft SC refers to a SC which does not completely stop the cycling, the cell recovers and run for some time, either with the same performance or not. This might for example occur when edges of the electrodes touch each due to movement by external pressure or other external or internal factors [37]. In Fig. 3.7., a) it is possible to observe the soft SC around 1.9 mAh/cm^2, and in b) it is possible to see how the cell eventually fails. The explanation for cell failure could be the formation of dendrites that penetrate through the Celgard separator.

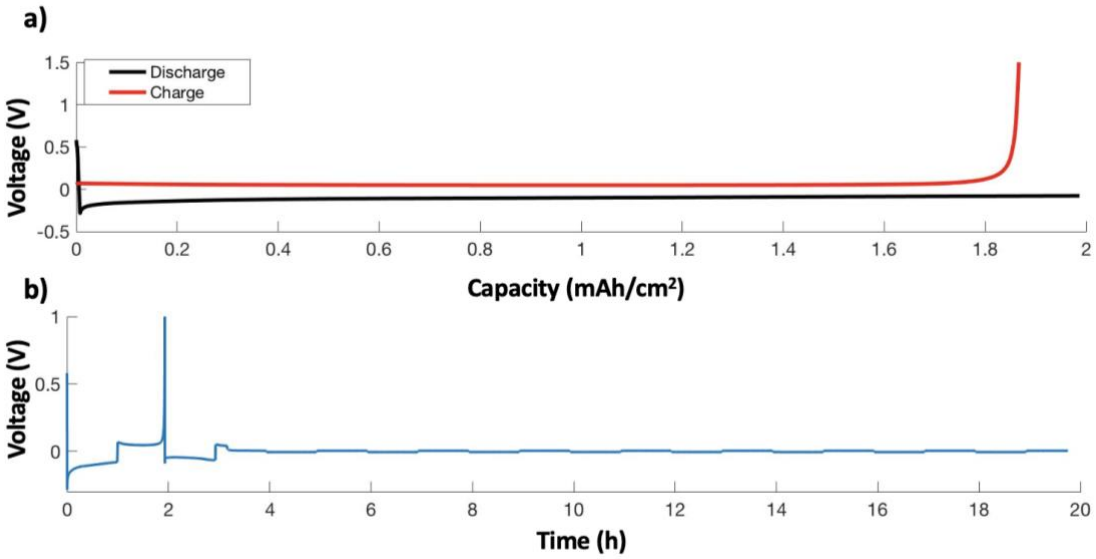

Fig. 3.8. Rate tests with 0.25 M $LiNO_3$ in the electrolyte with Celgard-Whatman-Celgard set-up a) First cycle b) Full voltage profile

After unsuccessful attempts to run the cell at 2 mA/cm^2, the design of the cell was changed. Instead of one Celgard separator, a Whatman glass fiber separator sandwiched between two Celgard separators to increase the distance between electrodes and an increased electrolyte volume was used. The results of this test in Fig. 3.8. a) show a successful first cycle with no signs of failing; in the second cycle a short-circuit is seen (Fig. 3.8. b). The procedure was modified to start with a lower current density and gradually increase the current density to 2 mA/cm^2 to avoid short circuits. This approach was successful with the Celgard/Whatman/Celgard separator set-up.

In Fig. 3.9., the coulombic efficiency is compared for different rates for cells without and with 0.25 M $LiNO_3$. Apparently, the gradual current density increase ensured a goal SEI formation, allowing the cell to run successfully at higher rates [42]. One can note that by increasing the current density, the coulombic efficiency decreases. However, when adding $LiNO_3$ to the electrolyte, the coulombic efficiency at the rate of 2 mA/cm^2 is higher (~80 %) than for the cell with no $LiNO_3$ (~65 %).

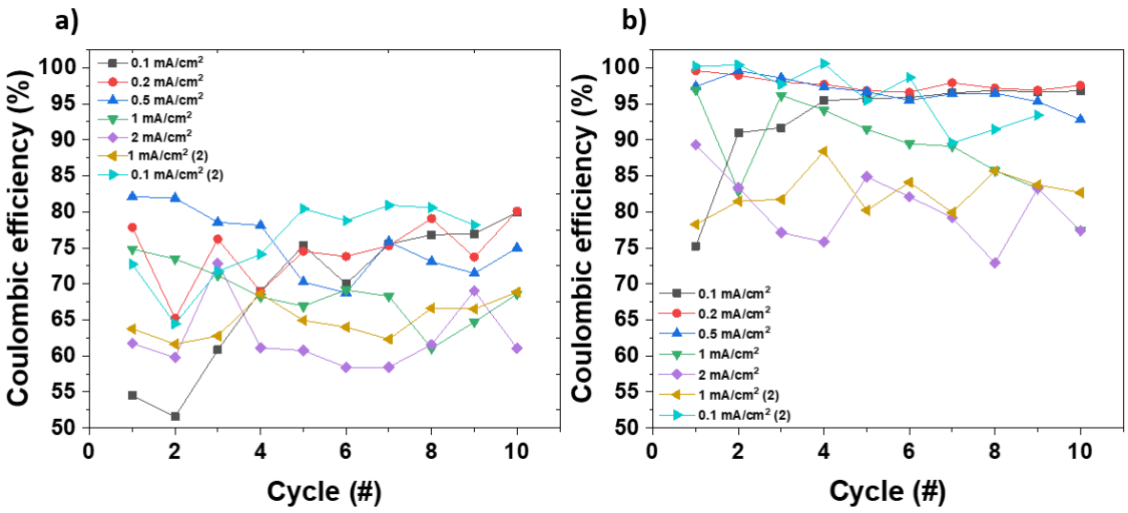

Fig. 3.9. Coulombic efficiency with gradual increase and decrease: a) Cells without $LiNO_3$ in electrolyte; b) Cells with 0.25 M $LiNO_3$ in electrolyte

3.1.3. Pre-deposition test

In Fig. 3.10, where Li was pre-deposited, the cell with $LiNO_3$ in electrolyte was able to run at 100 % CE, however after 20 cycles CE rapidly decreased to 97.5 %. The drop in CE could be explained by the consumption of $LiNO_3$ for SEI formation or other side reactions. The CE of the cell without $LiNO_3$ increased very slowly and remained very unstable.

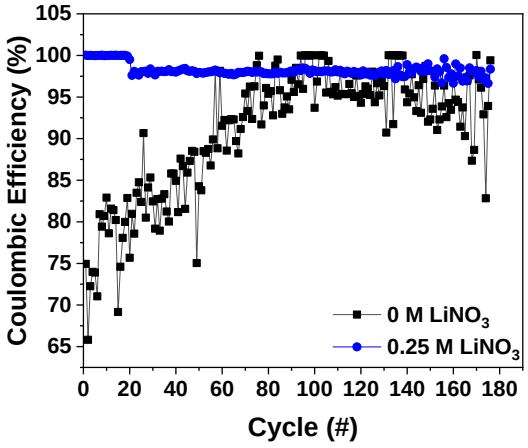

Fig. 3.10. Coulombic efficiency for cells with Li pre-deposition

3.1.4. Exchange current density calculations

Table. 3.1.

$LiNO_3$ concentration	Repeat	Exchange current (µA)	
		Instant measure	Pre-cycled
0 M	1	540	270
	2	2700	540
0.25 M	1	280	900
	2	400	1100
0.5 M	1	340	330
	2	0	360

Results obtained for the exchange current density are shown in Table. 3.1. Comparing exchange current for pre-deposited cells and pristine cells and with different $LiNO_3$ concentrations, no trend could be observed, and results are not reproducible. That might be due to difficulties of isolating parameters of this complex electrochemical system, such as an interface that is formed is very time-sensitive, pressure in the cell varies, the surface of the lithium and others [37].

3.2. *Operando* X-ray Tomography Microscopy

To obtain binary images of lithium deposits, appropriate settings for tomograms had to be applied. As explained in the methodology section, tomograms were first cropped to select an active area, Fig. 3.11. To remove any background noise, filters were applied. To assess which filter to use, it was necessary to consider filter resolution and Fig. 3.11. shows some examples of the effect of different filter settings.

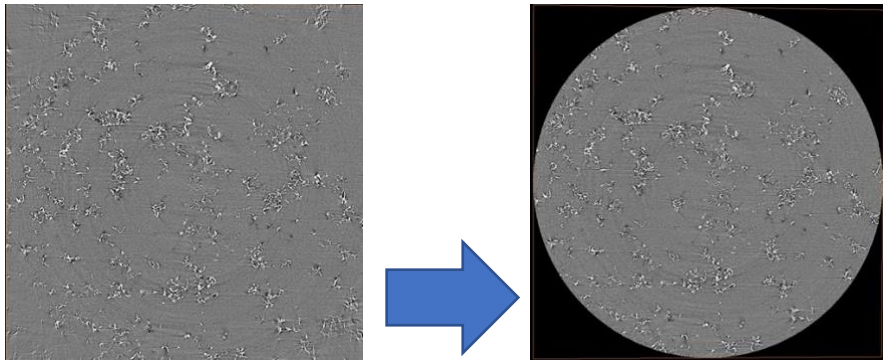

Fig. 3.11. Applying Mask setting to remove data from corners

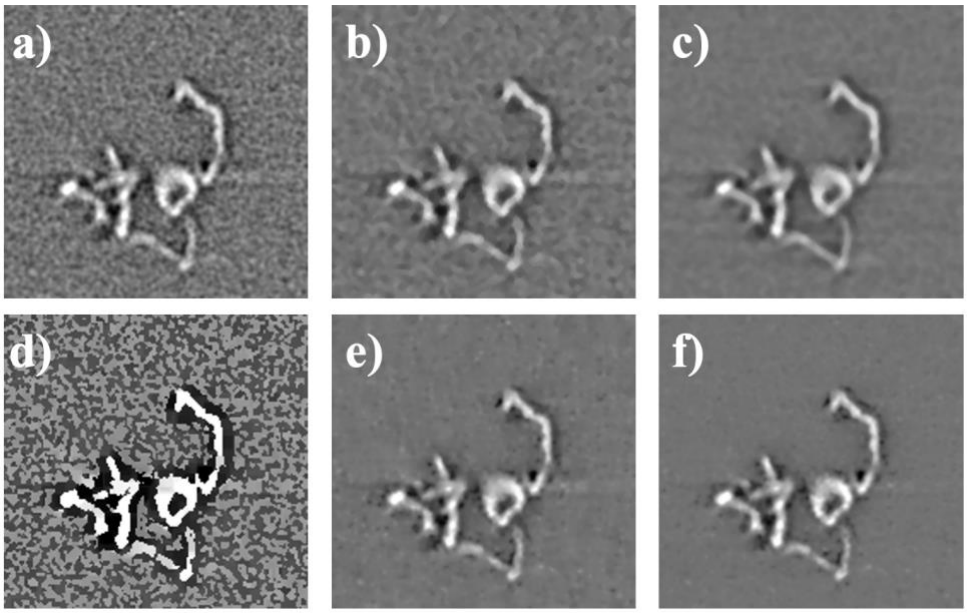

Fig. 3.12. a) No filter; b) 2D Median; c) 3D Median; d) 3D Delineate; e) 2D Non-local means; f) 3D Non-local means.

As the main aim of applying a filter is to lower the background noise, taking a look at the images in Fig. 3.12. it is possible to observe how with the Delineate filter, background noise is still present even though it shows the highest resolution (Fig. 3.13.). Comparing images with

no filter and with applied filters, such as Median and Non-local means, a significant difference in how the background is smoothened out and edges are emphasized can be noted. That proves that the application of a filter is required.

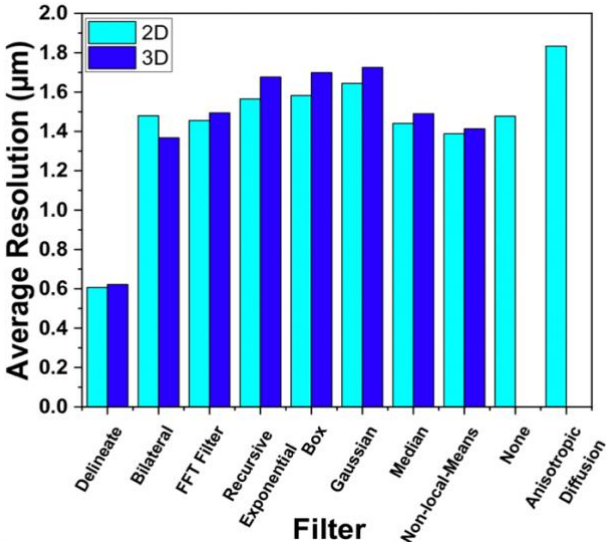

Fig. 3.13. Average resolution for each filter

Fig. 3.13. compares average resolution for different filters. Since Non-local-means (which gave the second-best resolution) resulted in slow processing, it was decided to use a Median filter. The effect of applying this filter to the tomograms is shown in Fig. 3.14.

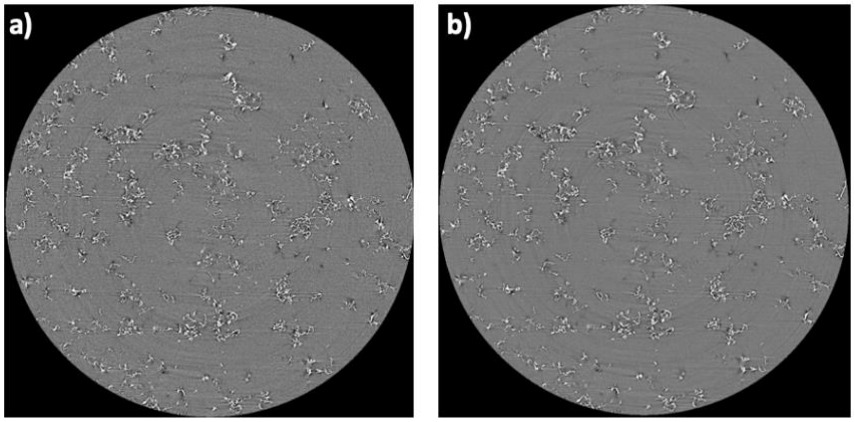

Fig. 3.14. Slice of a after discharge sample without $LiNO_3$ in electrolyte a) Non-filtered; b) Filtered by Median filter

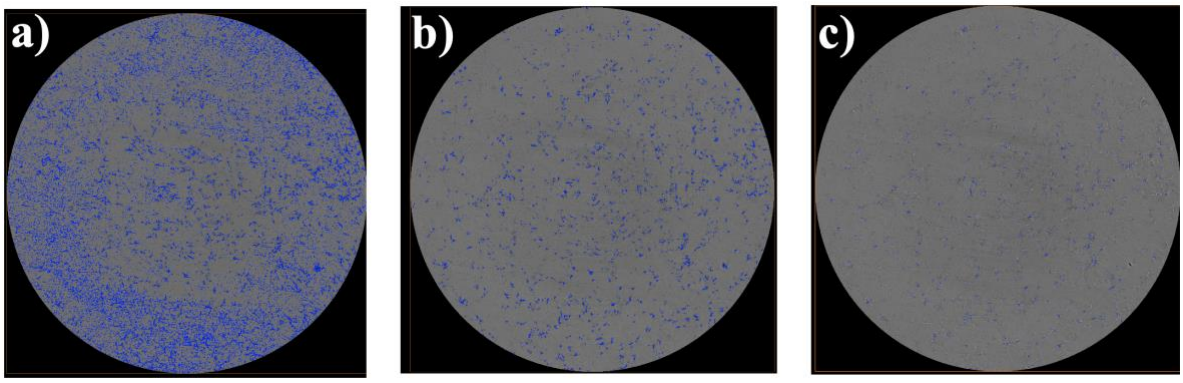

Fig. 3.15. Interactive thresholding for the slice of a after discharge sample without $LiNO_3$ in electrolyte – a) threshold too low; b) just right; c) too high.

In the segmentation stage, Fig. 3.15., it is vital to choose an appropriate threshold value to avoid background noise but not to lose any information. Fig. 3.16. shows how the number of disconnected structures varies by changing the threshold values. That was done to determine the best settings for data segmentation. The following values for thresholding were chosen – 37500 for 0 M $LiNO_3$ and 31500 for 0.25 M, whereas small spot removal – 200 px were chosen. These values were determined based on the value at the beginning of the plateaus of the thresholding plots, the amount of disconnected object did not change significantly anymore.

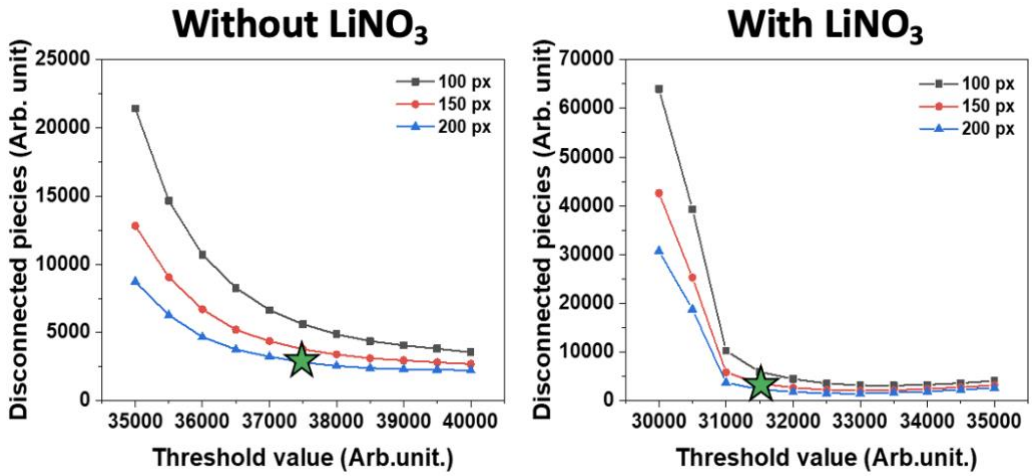

Fig. 3.16. Determination of segmentation settings

After segmentation, binary images with only lithium could be exported, as shown in Fig. 3.17. Figs. 3.17. a and d show the segmentations of the pristine electrode (bare Cu). In Fig. 3.17. b and e plated Li is observed and a clear difference in the morphology is seen. When lithium nitrate was not added to the electrolyte (Fig. 3.17. b) dendrites are significant and the

deposition is uneven, whereas with 0.25 M $LiNO_3$ in the electrolyte (Fig. 3.17. e) deposits are very uniform and dense. After charge (Fig. 3.17. c and f), it can be seen that all the lithium is not stripped from the copper, but deposits remain and are still more uniform with 0.25 M $LiNO_3$ added to the electrolyte.

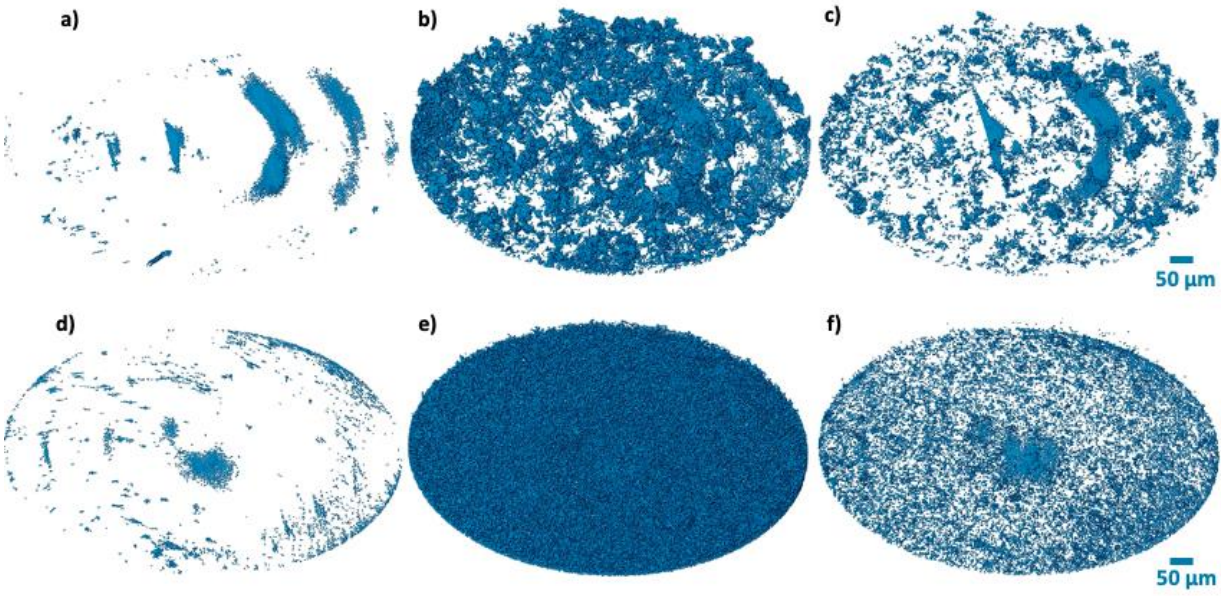

Fig. 3.17. Lithium deposit evolution: a, b, c – without $LiNO_3$; d), e), f) – 0.25 M $LiNO_3$; a), d) – Pristine electrodes; b), e) – After discharge (plated); c), f) – After-charge (stripped)

From binary images, precise quantitative values of voxel amount could be obtained, representing the volume of lithium deposits. To exclude preliminarily background noise, voxels of pristine electrodes were subtracted from the rest of the data. Therefore, a quantification of the lithium volume after discharge and after charge could be performed (Fig. 3.18.). It can be observed that during discharge, the volume of the plated lithium is much higher for the cell with 0.25 M $LiNO_3$. In Fig. 3.18. b) the voxel amount during charge is normalized with respect to the voxel count of the discharge. It can be observed that with $LiNO_3$ the relative amount of stripped lithium is higher than without $LiNO_3$.

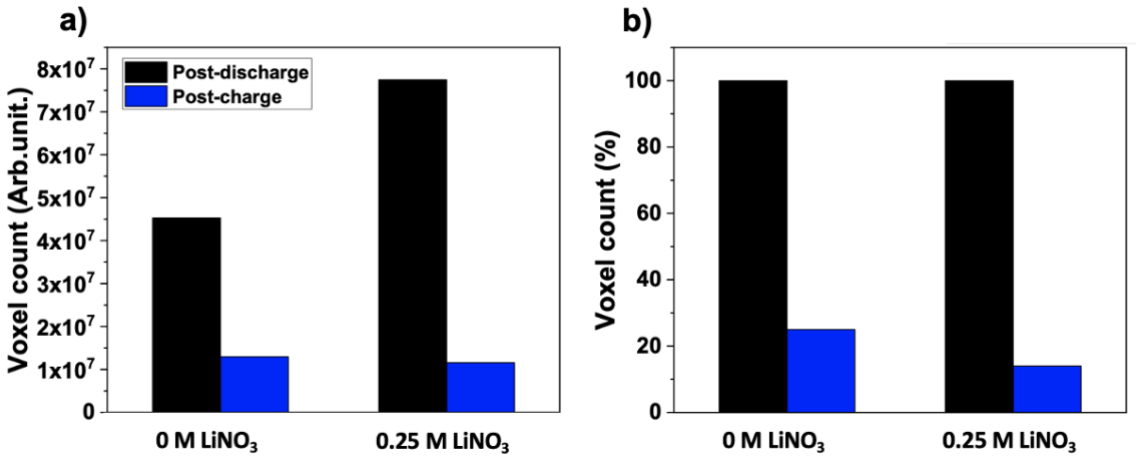

Fig. 3.18. a) Amount of Li deposits in voxels; b) Amount of Li deposits normalized to the voxel count after discharge

CONCLUSIONS AND OUTLOOK

The impact of $LiNO_3$ as additive to the electrolyte in Li-metal batteries was investigated. It was observed that with an increase of $LiNO_3$ concentration, the coulombic efficiency and cycling stability were increased. Also, with the highest concentration of $LiNO_3$ (0.5 M) the overvoltage was lower. From a comparison of cells with various lithium nitrate concentrations, consumption of lithium nitrate during cycling can be inferred.

Operando Tomographic Microscopy imaging was performed to study the effect on the morphology of deposited Li-metal by the addition of $LiNO_3$. The morphology change after discharge and charge showed a clear difference between the systems with and without $LiNO_3$ added to the electrolyte. With 0.25 M $LiNO_3$ added, lithium deposits were much more uniform and dense. During discharge a higher amount of lithium could be plated, and a higher amount of lithium could also be stripped.

For further studies, first, it would be interesting to analyse results from tomography datasets that were obtained through each 10 minutes of deposition and stripping, also at high rate (2 mA/cm^2), and see how the lithium morphology evolves during plating and stripping with various $LiNO_3$ concentrations and also the influence of the applied current densities. With the help of distinguishing separate structures during segmentation, would be a valuable opportunity to identify dead lithium. Complementary, it would be worthwhile to investigate more characteristics of the SEI formed for different lithium nitrate concentration with the help of other methods such as XPS, FTIR, TEM or EIS and link the difference of the SEI with respect to cell reversibility and life-span.

Regarding data processing, it is important to have a systematic approach to the treatment of the tomography data during filtering and thresholding as such processes when done manually are very subjective. To exclude any human error, it might be possible to involve machine learning for segmentation stage in the future.

REFERENCES

1. Larcher, D. & Tarascon, J. M. Towards greener and more sustainable batteries for electrical energy storage. *Nat. Chem.* **7**, 19–29 (2015).
2. Zhang, Y. *et al.* Towards better Li metal anodes: Challenges and strategies. *Mater. Today* **33**, 56–74 (2020).
3. Palacin, M. R. Battery Materials Design Essentials. *Accounts Mater. Res.* (2021) doi:10.1021/accountsmr.1c00026.
4. Chawla, N., Bharti, N. & Singh, S. Recent advances in non-flammable electrolytes for safer lithium-ion batteries. *Batteries* **5**, (2019).
5. Liu, Y. *et al.* Insight into the Critical Role of Exchange Current Density on Electrodeposition Behavior of Lithium Metal. *Advanced Science* vol. 8 (2021).
6. Lin, D., Liu, Y. & Cui, Y. Reviving the lithium metal anode for high-energy batteries. *Nat. Nanotechnol.* **12**, 194–206 (2017).
7. Liu, J. *et al.* Pathways for practical high-energy long-cycling lithium metal batteries. *Nat. Energy* **4**, 180–186 (2019).
8. Jin, H., Liu, H., Cheng, H., Zhang, P. & Wang, M. The synergistic effect of lithium bis(fluorosulfonyl)imide and lithium nitrate for high-performance lithium metal anode. *J. Electroanal. Chem.* **874**, 114484 (2020).
9. EUCAR. Battery requirements for future automotive applications. *Eg Bev&Fcev* 1–18 (2019).
10. Tan, C. *et al.* Four-Dimensional Studies of Morphology Evolution in Lithium-Sulfur Batteries. *ACS Appl. Energy Mater.* **1**, 5090–5100 (2018).
11. Lewis, J. A. *et al.* Linking void and interphase evolution to electrochemistry in solid-state batteries using operando X-ray tomography. *Nat. Mater.* **20**, 503–510 (2021).
12. Derek Pletcher. *A First Course in Electrode Processes*. (2009).
13. Biswal, P., Stalin, S., Kludze, A., Choudhury, S. & Archer, L. A. Nucleation and Early Stage Growth of Li Electrodeposits. *Nano Lett.* **19**, 8191–8200 (2019).
14. Lu, J., Chen, Z., Pan, F., Cui, Y. & Amine, K. High-Performance Anode Materials for Rechargeable Lithium-Ion Batteries. *Electrochem. Energy Rev.* **1**, 35–53 (2018).
15. Hong, X. *et al.* Nonlithium Metal–Sulfur Batteries: Steps Toward a Leap. *Adv. Mater.* **31**, 1–30 (2019).
16. Xiao, J. *et al.* Understanding and applying coulombic efficiency in lithium metal batteries. *Nature Energy* vol. 5 561–568 (2020).

17. Qian, J. *et al.* High rate and stable cycling of lithium metal anode. *Nat. Commun.* **6**, (2015).
18. Pei, A., Zheng, G., Shi, F., Li, Y. & Cui, Y. Nanoscale Nucleation and Growth of Electrodeposited Lithium Metal. *Nano Lett.* **17**, 1132–1139 (2017).
19. Biswal, P. *et al.* The early-stage growth and reversibility of Li electrodeposition in Br-rich electrolytes. *Proc. Natl. Acad. Sci. U. S. A.* **118**, 1–11 (2021).
20. Armand, J.-M. T. & M. Issues and challenges facing rechargeable lithium batteries. *Nature* **414**, 359–367 (2001).
21. Yan, C. *et al.* Lithium Nitrate Solvation Chemistry in Carbonate Electrolyte Sustains High-Voltage Lithium Metal Batteries. *Angew. Chemie - Int. Ed.* **57**, 14055–14059 (2018).
22. Olof Ramström. Scientific Background on the Nobel Prize in Chemistry 2019: LITHIUM-ION BATTERIES. https://www.nobelprize.org/uploads/2019/10/advanced-chemistryprize2019.pdf (2019).
23. Wieboldt, D. & Hahn, M. In situ Raman Analysis of Lithium Ion Batteries. *ThermoScientific Appl. Note* 52676 (2015).
24. Cadex. Types of lithium ion batteries. https://batteryuniversity.com/learn/article/types_of_lithium_ion (2021).
25. Manthiram, A. A reflection on lithium-ion battery cathode chemistry. *Nat. Commun.* **11**, 1–9 (2020).
26. Casimir, A. *et al.* Silicon-based anodes for lithium-ion batteries: Effectiveness of materials synthesis and electrode preparation. *Nano Energy* **27**, 359–376 (2016).
27. Liu, Q. *et al.* Enhanced ionic conductivity and interface stability of hybrid solid-state polymer electrolyte for rechargeable lithium metal batteries. *Energy Storage Mater.* **23**, 105–111 (2019).
28. Xiao, J. How lithium dendrites form in liquid batteries. *Science* vol. 366 426–427 (2019).
29. Bai, P., Li, J., Brushett, F. R. & Bazant, M. Z. Transition of lithium growth mechanisms in liquid electrolytes. *Energy Environ. Sci.* **9**, 3221–3229 (2016).
30. Fang, C. *et al.* Quantifying inactive lithium in lithium metal batteries. *Nature* **572**, 511–515 (2019).
31. Peled, E. & Menkin, S. Review—SEI: Past, Present and Future. *J. Electrochem. Soc.* **164**, A1703–A1719 (2017).
32. Aleshin, A., Bravo, S., Redquest, K. & Wood, K. N. Rapid oxidation and reduction of

lithium for improved cycling performance and increased homogeneity. *ACS Applied Materials and Interfaces* vol. 13 2654–2661 (2021).

33. Ue, M. & Uosaki, K. Recent progress in liquid electrolytes for lithium metal batteries. *Current Opinion in Electrochemistry* vol. 17 106–113 (2019).
34. Ding, N. *et al.* Building better lithium-sulfur batteries: From LiNO2 to solid oxide catalyst. *Sci. Rep.* **6**, 1–10 (2016).
35. Yang, C. P., Yin, Y. X., Zhang, S. F., Li, N. W. & Guo, Y. G. Accommodating lithium into 3D current collectors with a submicron skeleton towards long-life lithium metal anodes. *Nat. Commun.* **6**, (2015).
36. Wood, K. N. *et al.* Dendrites and pits: Untangling the complex behavior of lithium metal anodes through operando video microscopy. *ACS Cent. Sci.* **2**, 790–801 (2016).
37. Fang, C. *et al.* Pressure-tailored lithium deposition and dissolution in lithium metal batteries. *arXiv* 1–12 (2020).
38. Denmark, T. U. of. Introduction to advanced tomography. *Course* https://www.coursera.org/learn/cinemaxe/home/welcome (2020).
39. Soltani, P., Johari, M. S. & Zarrebini, M. 3D fiber orientation characterization of nonwoven fabrics using X-ray micro-computed tomography. *World J. Text. Eng. Technol.* **1**, 41–47 (2015).
40. Birkl, C. R., McTurk, E., Roberts, M. R., Bruce, P. G. & Howey, D. A. A Parametric Open Circuit Voltage Model for Lithium Ion Batteries. *J. Electrochem. Soc.* **162**, A2271–A2280 (2015).
41. Chen, J. *et al.* Tuning the solution structure of electrolyte for optimal solid-electrolyte-interphase formation in high-voltage lithium metal batteries. *J. Energy Chem.* **60**, 178–185 (2021).
42. Zheng, G. *et al.* Interconnected hollow carbon nanospheres for stable lithium metal anodes. *Nat. Nanotechnol.* **9**, 618–623 (2014).

SUPPLEMENTARY INFORMATION

Supplement 1 – Full voltage profile of 0 M $LiNO_3$ cell

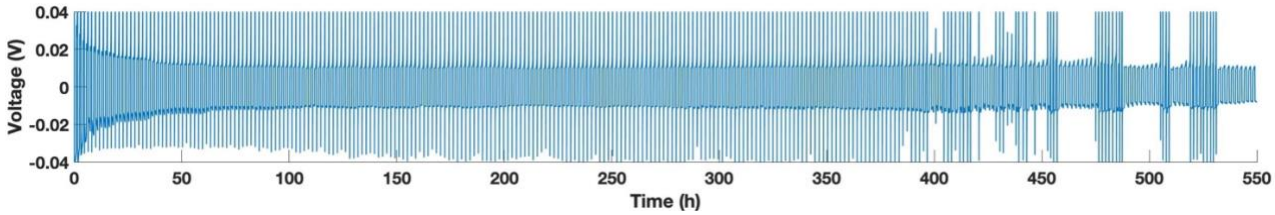

Supplement 2 – Full voltage profile of 0.1 M $LiNO_3$ cell

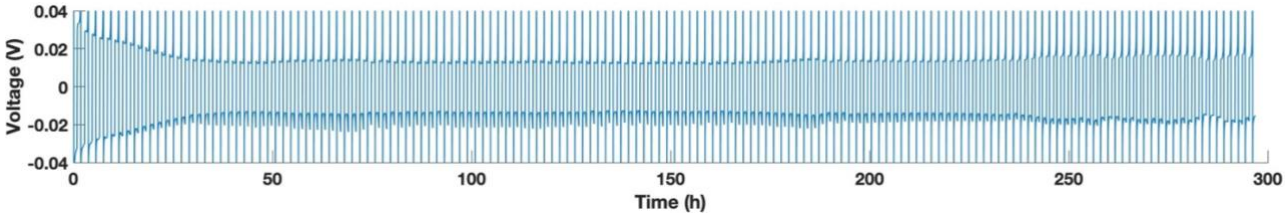

Supplement 3 – Full voltage profile of 0.25 M $LiNO_3$ cell

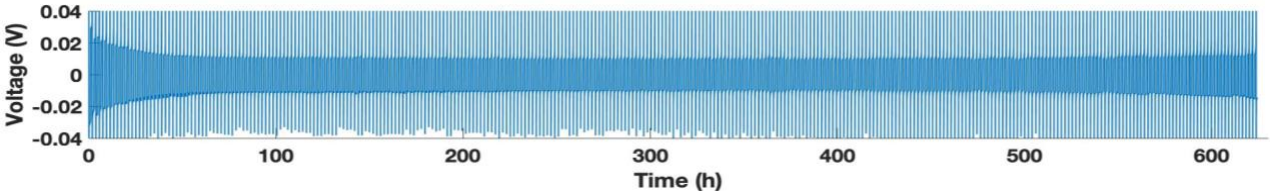

Supplement 4 – Full voltage profile of 0.5 M $LiNO_3$ cell

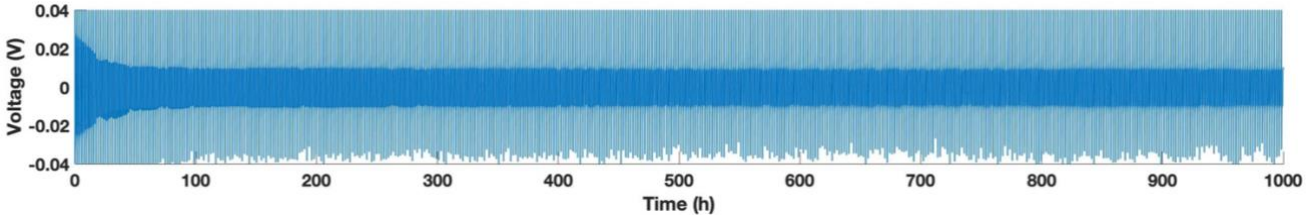

DEPARTMENT OF PHYSICS
CHALMERS UNIVERSITY OF TECHNOLOGY
Gothenburg, Sweden 2021
www.chalmers.se